# 15-year variability of desert dust optical depth on global and regional scales

Stavros-Andreas Logothetis[1], Vasileios Salamalikis[1], Antonis Gkikas[2] Stelios Kazadzis[3,4], Vassilis Amiridis[2] and Andreas Kazantzidis[1]

[1]Laboratory of Atmospheric Physics, Department of Physics, University of Patras, 26500 Patras, Greece
[2]Institute for Astronomy, Astrophysics, Space Applications and Remote Sensing, National Observatory of Athens, Athens, 15236, Greece
[3]Physics - Meteorology Observatory Davos, Word Radiation Center, Switzerland
[4]Institute of Environmental Research and Sustainable Development, National Observatory of Athens, Greece

*Correspondence to*: Andreas Kazantzidis (akaza@upatras.gr)

**Abstract.** This study aims to investigate the global, regional and seasonal temporal dust changes as well as the effect of dust particles on total aerosol loading, using the Modis Dust AeroSol (MIDAS) fine resolution dataset. MIDAS delivers dust optical depth (DOD) at fine spatial resolution (0.1° x 0.1°) spanning from 2003 to 2017. Within this study period, the dust burden has been increased across Central Sahara (up to 0.023 $yr^{-1}$) and Arabian Peninsula (up to 0.024 $yr^{-1}$). Both regions observed their highest seasonal trends in summer (up to 0.031 $yr^{-1}$). On the other side, declining DOD trends are encountered in Western (down to −0.015 $yr^{-1}$) and Eastern (down to −0.023 $yr^{-1}$) Sahara, Bodélé Depression (down to −0.021 $yr^{-1}$), Thar (down to −0.017 $yr^{-1}$) and Gobi (down to −0.011 $yr^{-1}$) Deserts and Mediterranean Basin (down to −0.009 $yr^{-1}$). At spring, the most negative seasonal trends are recorded in Bodélé Depression (down to −0.038 $yr^{-1}$) and Gobi Desert (down to −0.023 $yr^{-1}$) whereas in West (down to −0.028 $yr^{-1}$) and East Sahara (down to −0.020 $yr^{-1}$), and Thar Desert (down to −0.047 $yr^{-1}$) at summer. Over western and eastern sector of Mediterranean Basin, the most negative seasonal trends are computed at summer (down to −0.010 $yr^{-1}$) and spring (down to −0.006 $yr^{-1}$), respectively. The effect of DOD on the total aerosol optical depth (AOD) change is determined by calculating the DOD to AOD trends ratio. Over Sahara Desert the median ratio values range from 0.83 to 0.95 whereas in other dust affected areas (Arabian Peninsula, South Mediterranean, Thar and Gobi Deserts) the ratio value is approximately 0.6. In addition, a comprehensive analysis of the factors effecting the sign, the magnitude and the statistical significance of the calculated trends is conducted. Firstly, the implications between the implementation of geometric mean instead of arithmetic mean to trend calculations are discussed revealing that the arithmetic-based trends tend to overestimate compared with the geometric-based trends both over land and ocean. Secondly, an analysis interpreting the differences in trend calculations under different spatial resolutions (fine and coarse) and time intervals is conducted.

## 1 Introduction

Dust particles emitted from natural or anthropogenic sources are a major contributor to the atmospheric aerosol burden in terms of mass (Zender et al. 2004; Textor et al., 2006; Kok et al., 2017). Among aerosol properties, AOD describes adequately aerosols' load, in optical terms, corresponding to the entire atmospheric column. The proportion of AOD attributed to dust particles consists the DOD. The spatiotemporal patterns of mineral particles are determined by the dust life cycle components, characterized by a pronounced heterogeneity (Mahowald et al., 2014). The main natural dust sources are located in the northern hemisphere (Goudie and Middleton., 2006), with Sahara region being the most dominant one (Prospero et al., 2002; Goudie and Middleton, 2006; Rajot et al., 2008; Alizadeh-Choobari et al., 2014a). Other active source areas of mineral particles are situated in the Middle East and the region stretching from Mesopotamia to the Oman coasts in south Arabian Peninsula (Prospero et al., 2002; Ginoux et al., 2012), in southwest Asia and Sistan Basin (Iran-Pakistan-Afghanistan) (Alizadeh-Choobari et al., 2014b; Rashki et al., 2015), in Central Asia across the Karakum (Turkmenistan-Uzbekinstan) and Kyzylkum Deserts (southeast of the Aral sea in Uzbekistan) (Elguindi et al., 2016), in East Asia with Taklamakan (Tarim basin in northwest China) and Gobi (north China – south Mongolia) deserts (Ginoux et al., 2012), and in North America with Black Rock and Smoke, Great Salt Lake, and Chihuahuan and Sononan deserts (Ginoux et al., 2012).

Mineral dust aerosols are uplifted, accumulated into the atmosphere, and transported over enormous distances (up to some thousands of kilometers) from their sources (Goudie and Middleton., 2006) driven by the prevailing winds. Schepanski et al. (2018) reported that the transport distance of dust particles is strongly related to their residence time, which is analogous to the dust lifetime, dust layer altitude, atmospheric circulation pattern, buoyancy and gravitational forces. van der Does et al. (2018) also denoted that strong winds, turbulence, electrostatic forces developed by dust particles' charging, and thunderstorms or tropical cyclones may potentially enhance the residence time of dust aerosols into the atmosphere. On a seasonal basis, dust particles can be transported from north Africa towards the Atlantic Ocean reaching Caribbean, Central America, southern United States (in boreal summer) and South America (in spring and winter) (Griffin et al., 2002; Prospero and Lamb., 2003; Kalashnikova et al., 2008; Huang et al., 2010; Tsamalis et al., 2013; Prospero and Mayol-Bracero., 2013). Additionally, Saharan dust is advected towards the Mediterranean and Europe (Mona et al., 2006; 2012, Papayannis et al., 2008; Basart et al., 2009; Schepanski et al., 2018; Gkikas et al. 2015, 2016, Logothetis et al., 2020, 2021).

During the last decades, numerous studies have been conducted using observations from various satellite sensors. Prospero et al. (2002) and Ginoux et al. (2012) identified the global dust sources relying on Total Ozone Mapping Spectrometer (TOMS, Torres et al., 2002) and Moderate Resolution Imaging Spectroradiometer (MODIS, Remer et al., 2008), respectively. More specifically, the studies of Prospero et al. (2002) and Ginoux et al. (2012) were based on the frequency of occurrence (FoO) of TOMS absorbing aerosol index (AAI) and MODIS-based DOD, respectively, exceeding defined thresholds. In addition, Ginoux et al. (2012) associated the dust frequency with three clusters such as hydrologic and non-hydrologic natural or anthropogenic in order to distinguish the dust origin. Similarly, at a regional scale, Schepanski et al. (2012) implemented a comprehensive analysis on the potential differences of Saharan dust active sources within the intercomparison of aerosol properties observations derived from MODIS, Meteosat Second Generation (MSG) and Ozone Monitoring Instruments (OMI). Voss and Evan (2020) presented a global DOD climatology, both over land and ocean, using MODIS (Aqua and Terra) from 2001 to 2018 and Advanced Very High Resolution Radiometer (AVHRR) over ocean from 1981 to 2018. Similarly, Clarisse et al. (2019) performed a global seasonal DOD climatology relying on Infrared Atmospheric Sounding Interferometer (IASI) retrievals, during the 2008−2017. Yu et al. (2019), derived DOD using MODIS, IASI and Multiangle Imaging Spectroradiometer (MISR) and in conjunction with dust vertical profiles from Cloud−Aerosol Lidar with Orthogonal Polarization (CALIOP) (Shikwambana and Sivakumar., 2018) investigated the dust deposition and loss frequency across the Tropical Atlantic Ocean on a seasonal basis.

The investigation of dust loads' variation at interannual time scales is quite critical for assessing the associated impacts on climate as well as the response of these tendencies to environmental factors. Since the majority of remote sensing instruments provide an AOD product, numerous studies on a global scale, are focused on the estimation of AOD temporal trends, which are not always representative of DOD, being mixed with other aerosol types (Zhang and Reid, 2010; de Meij et al., 2012; Hsu et al., 2012; Yoon et al., 2014; Pozzer et al., 2015; Alfaro-Contreras et al., 2017; Zhao et al., 2017; Che et al., 2019) and regional scales (Guo et al., 2011; Li, 2014; Klingmüller et al., 2016; Floutsi et al., 2016; Dahutia et al., 2017; Hu et al., 2018; Zhang et al., 2018). Limited satellite studies are dedicated to the estimation of DOD temporal trends due to the deficiency to quantify accurately the portion of AOD attributed to DOD. Prior studies have investigated the interannual patterns of DOD over the "dusty" regions of the planet. Dust load has been increased across the Sahara Desert, based on MODIS-Aqua derived DOD dataset during 2003−2018 (Voss and Evan 2020). Notaro et al. (2015) detected a regime shift in dust activity between 1998−2005 (inactive dust period) and 2007−2013 (active dust period) across Arabian Peninsula, which is attributed to the prolonged drought along the Fertile Crescent. Through the synergy of MISR DODs and back trajectories, they revealed that the positive DOD anomalies (increased dust burden) are strongly connected with dust advection from the Fertile Crescent towards the Arabian Peninsula. These findings are consistent with the strong positive AOD (Klingmüller et al., 2016) and DOD (Voss and Evan 2020) trends reported in the area. Voss and Evan (2020), found a reduction of dust load across the Northern African coasts over the period 2001−2018, based on MODIS-Terra DOD dataset. Declining DOD trends have also been reported in Central Asia by Xi and Sokolik (2015), who analyzed MODIS and Sea-viewing Wide Field-of-view Sensor (SeaWiFs) DODs for a 15-year period (2000-2014). DOD trend sign is also abruptly changed from positive (1999-2009) to negative (2010−2016) over East Asia and North Pacific Ocean in springtime, based on Modern-Era Retrospective Analysis for Research and Applications, Version 2 (MERRA-2) (Gelaro et al., 2017) measurements (Guo et al., 2019). Across South Asia, a negative shift in DOD interannual variation is recorded during the pre-monsoon season between 2008–2012 and 2013–2017, based on CALIOP observations (Lakshmi et al., 2019). In the southern sector of the Gobi Desert, declining DOD trends are observed from MODIS and CALIOP DOD datasets during 2007−2019 (Song et al., 2021).

This study's main objective is to investigate the dust temporal variations at global, regional, and seasonal scales, using the newly MIDAS DOD product from 2003–2017. A few aspects regarding the innovative points of this research are highlighted below to support the scientific contribution to the relevant research field. First, in contrast to the existing studies, this trend analysis relies on fine spatial resolution data, making it feasible to depict in detail the spatial patterns of the DOD variations. Such information can be critical for interpreting the perturbations of the radiation fields, environmental impacts, and health effects attributed to dust particles. One more advantage of the high resolution DOD analysis is the flexibility of the final grid size selection depending on data availability, which is a critical aspect when satellite observations are used. MIDAS data can be easily upscaled at coarser spatial resolutions in order to match spaceborne observations, which have been commonly used in other trend analyses available in the literature (Hsu et al., 2012; Yoon et al., 2014; Notaro et al., 2015; Pozzer et al., 2015; Klingmüller et al., 2016; Alfaro-Contreras et al., 2017; Che et al., 2019; Guo et al., 2019; Voss and Evan 2020; Song et al., 2021). In addition, fine spatial resolution data ensure a more realistic collocation with ground-based measurements for validating the obtained DOD trends. Second, quite a few studies concentrate on pure DOD (Xi and Sokolik 2015; Guo et al., 2019; Lakshmi et al., 2019; Voss and Evan 2020; Song et al., 2021) rather than AOD to analyze the trends of mineral particles' load. Even though the consideration of the latter parameter is quite reasonable across deserts, its representativeness over downwind areas is questionable due to the coexistence of other aerosol types. Such types can also affect the DOD trend uncertainty. In MIDAS, this issue is addressed by the adjustment of MODIS AOD to DOD in terms of the MERRA-2 dust fraction, while in other studies, aerosol size and natural optical properties, which their quality above land is downgraded, are used in parallel. Third, taking advantage that MIDAS provides DOD and quality assured AOD, their trends are discussed jointly for assessing the contribution of dust burden temporal variations to those of the total aerosol load. It should be mentioned that this is the first study assessing the effect of DOD to total AOD trends across the major desert dust areas of the planet, highlighting the potential role of desert dust particles in past, present, and future AOD trend studies. Fourth, the investigation of the potential impact on trends' magnitude, sign, and statistical significance when different DOD aggregations (i.e. arithmetic mean vs. geometric mean) are considered among various spatial and temporal scales. Fifth, the DOD interannual variations are discussed for the entire study period on a seasonal basis and sub-periods for detecting alternations on DOD trends within the period of interest.

The current paper is organized as follows. Sect. 2 describes the (i) MIDAS (Sect. 2.1) and (ii) AERONET (Sect. 2.2) datasets as well as the trend detection methodology (Sect. 2.3). The results section (Sect. 3) is divided into three sub-sections analyzing (i) the global AOD and DOD tendencies (3.1), along with the sensitivity analyses between arithmetic and geometric means (3.1.1), fine (0.1° x 0.1°) and coarse (1° x 1°) spatial resolutions (Sect. 3.1.2), MIDAS DOD and AEROENT retrievals (Sect. 3.1.3), and filtered and non-filtered data trend calculations (Sect. 3.1.4), (ii) global dust temporal trends on a seasonal basis (Sect. 3.2), and (iii) DOD temporal tendencies into specific regions (Sect. 3.3). Finally, a discussion focusing on the main findings of this study is presented in the summary and conclusion section (Sect. 4). The current study represents a practical implementation of the MIDAS dataset and aims to demonstrate its feasibility on the estimation of dust load variation at various temporal and spatial scales.

## 2 Data and Methods

### 2.1 Modis Dust AeroSol (MIDAS) dataset

MIDAS dataset (Gkikas et al., 2021a) provides columnar DOD at 550 nm, on a daily basis over the 15-year period spanning from 2003 to 2017, at a global scale and fine spatial resolution (0.1° x 0.1°). Its development has relied on the synergistic implementation of quality filtered AOD retrievals from MODIS-Aqua (Level 2; Collection 6.1) and MERRA-2 dust fraction (MDF), both reported at 550 nm. More specifically, the multiplication of MODIS-Aqua AOD with MDF provides the MIDAS-DOD on MODIS native grid which is converted to an equidistant lat-lon projection. In order to justify the reliability of MDF, it has been evaluated against the corresponding portion provided by the LIVAS database (Amiridis et al., 2013; 2015). Based on the aforementioned assessment analysis, it has been revealed an adequate representation of MERRA-2 dust fraction, in optical terms, over the main dust sources and the outflow regions, in contrast to areas where dust presence is weak. MIDAS implements the MODIS aerosol products in which AOD is derived using the Dark Target (DT) and Deep Blue (DB) algorithms. Globally, these products have been thoroughly validated against AERONET, providing a very good agreement either over oceanic areas for DT (R=0.880; MAE=0.055; RMSE=0.083) or over land for DT (R=0.920; MAE=0.066; RMSE=0.107) and DB (R=0.904; MAE=0.062; RMSE=0.107) (Wei et al., 2019b). Therefore, the combination of highly accurate MODIS AODs (Wei et al., 2019b) and quite reliable MDF results in a trustworthy MIDAS DOD product as it has been justified via its evaluation against AERONET dust-like AOD and its intercomparison versus DOD derived by LIVAS and MERRA-2. For the former analysis, the ground-based AODs have been treated appropriately in order to resemble DOD, as much as possible, assuming that the contribution of fine mineral particles is negligible and trying to minimize the contribution of non-dust aerosol species to the columnar aerosol load. Under these assumptions, the evaluation metrics, both at global and station level, reveal a quite high level of agreement between the two datasets. At global scale, there is a high level of agreement between MIDAS and AERONET DODs as indicated by the high correlation (~0.9) and the low positive bias (0.004 or 2.7%). Across the 'dust belt', the correlation coefficients can reach up to 0.98 at station level whereas positive biases (mostly lower than 0.06) are found. Outside of this zone, the correlation reduces, and the biases of similar magnitude are switching to negative. Likewise, it has been evident a considerable consistency among MIDAS, LIVAS and MERRA-2 DODs at global and hemispherical scales, despite the different approaches applied for the DOD derivation, whereas the intercomparison results are regionally dependent. Summarizing, the reliability of the MIDAS DOD justified in Gkikas et al. (2021a) strengthens its applicability for investigating the temporal trends of dust aerosol burden over long-time periods and at various spatial scales.

### 2.2 AERONET

On a regional basis, the reliability of MIDAS DOD trends has been evaluated using ground-based measurements from AERONET (Holben et al., 1998). AERONET provides information for the spectral columnar AOD using direct spectral solar irradiance. In addition, the physical and optical properties of aerosols can be derived by applying the Dubovik and King (2000) inversion algorithm. DOD ground-based measurements can be approached using AERONET retrievals, however, an aerosol classification scheme is mandatory. Through MIDAS evaluation procedure, the discrimination of dust load from non-dust aerosol species has been performed in terms of the Ångström wavelength exponent at 440-870 nm ($AE_{440\text{-}870\ nm}$) and the difference between single scattering albedo at 440 nm ($SSA_{440\ nm}$) and 675 nm ($SSA_{675\ nm}$). $AE_{440\text{-}870\ nm}$ has been used as an indicator of particles size (coarse or fine aerosols) in numerous aerosol classification studies (Basart et al., 2009; Mielonen et al., 2009; Lee et al., 2010; Giles et al., 2012; Hamill et al., 2016; Zheng et al., 2017; Che et al., 2018; Logothetis et al., 2020). In addition, the aerosols origin can be acquired using either the difference between SSA at different wavelengths or specific spectral SSA thresholds. In Gkikas et al. (2021a), the pure dust conditions have been succeeded using a very restricted threshold limit of $AE_{440\text{-}870}$ nm ($\leq 0.75$) along with a positive difference of $SSA_{675\ nm} - SSA_{440\ nm}$. Despite the favorable dust conditions retrieved through the SSA retrievals, the data availability strongly decreases causing difficulties in trend calculations. In the current study, the evaluation of MIDAS DOD trends is performed by using the AERONET coarse mode AOD at 500 nm, derived from the spectral deconvolution algorithm (SDA) (O'Neill et al., 2001, 2003). The performance of the SDA algorithm, in terms of segregating the fine and coarse aerosol modes, has been justified against ground-based observations (Kaku et al., 2014). Only quality assured data (cloud-screened), including pre-field and post-field calibrations (Level 2.0, L2) from AERONET Version 3 (V3) (Giles et al., 2019) are used. It should be mentioned that cAOD does not represent profoundly the dust load due to the presence of sea-salt particles.

### 2.3 Temporal trends methodology

The spatiotemporal changes of dust particles' burden, over the period 2003 – 2017, are investigated by calculating the annual trends derived by the monthly MIDAS DODs. At each grid-cell, the monthly DOD averages are calculated when the 20% ($\geq$ 6 days) of daily data are available (Hsu et al., 2012). Subsequently, at the grid points with more than 60 months available (5 out of 15 complete years) linear trends are calculated by the implementation of the following equation,

$$Y_t = \mu + S_t + \omega X_t + N_t \tag{1}$$

where $Y_t$ is the monthly averaged values, $\mu$ the offset term, $S_t$ is the seasonal term (i.e. long-term monthly value), $\omega$ the linear trend and $N_t$ the residuals. The seasonality is removed by subtracting $S_t$ from $Y_t$. The statistical significance of $\omega$ is derived according to Weatherhead et al. (1998). $N_t$ follows a 1$^{st}$-order autoregressive process (significant lag-1 autocorrelation),

$$N_t = \varphi N_{t-1} + \varepsilon_t \tag{2}$$

with $\varepsilon_t$ is the white noise and $\varphi$ the lag-1 autocorrelation coefficient. The standard deviation of the trend can be expressed as,

$$\sigma_\omega \approx \frac{\sigma_N}{n^{3/2}} \sqrt{\frac{1+\varphi}{1-\varphi}} \tag{3}$$

where $\sigma_N$ is the standard deviation of $N_t$ and n is the number of complete years depending on the data availability at each grid cell without always considering the entire period (i.e. a constant value of 15 years). When $|\omega/\sigma_\omega|>2$, significant temporal trends are considered at a 95% confidence level. The methodology of Weatherhead et al. (1998) is commonly applied in numerous studies concerning the detection of temporal trends in AOD (Hsu et al., 2012; Babu et al., 2013; Li et al., 2014; Kumar et al., 2015, 2018; Pozzer et al., 2015; Adesina et al., 2016; Alfaro-Contreras et al., 2017; Zhang et al., 2018; Ningombam et al., 2019). Additionally, for comparison purposes with previous studies, AOD and DOD linear trends are calculated also at 1° spatial resolution. The re-gridding procedure from fine to coarse spatial resolution is implemented following Levy et al. (2009) (upper branch in Fig. 5 of their publication). For the calculation of regional trends (Sect. 3.3), the same approach is adopted. First, daily spatial grids of 0.1° are temporally averaged to create monthly data. Then, monthly grids with 1° spatial resolutions are generated using a weighted aggregation of monthly fine grids. The weighting factors are defined in terms of latitude. More specifically, this weighting scheme considers the fraction between the area covered by each fine grid-cell to the total available surface area within the coarse grid-cell.

The appropriate selection of the statistical average metric (e.g. arithmetic or geometric mean) is reflected to the background probability distribution which the raw data are resembled. For instance, the vast majority of the studies focusing on AOD statistics have thoroughly consider that AOD follows a Gaussian distribution using the simple arithmetic mean for temporal and spatial aggregations. Nevertheless, the frequency distribution of AOD follows is more well fitted to the log-normal distribution (O' Neill et al., 2000). Sayer and Knobelspiesse (2019) designated that the calculation of the geometric instead of the arithmetic mean for obtaining temporal and spatial AOD trends may underestimate them comparing to those reported in the literature. Here, in order to investigate the potential differences on AOD and DOD temporal trends, a sensitivity analysis using both geometric and arithmetic mean is established. MIDAS dataset includes negative DOD values introduced from the applied Dark Target algorithm of MODIS AOD retrievals. Since zero or negative arguments of logarithm cannot be defined, all these values are overwritten to 0.0001 as suggested by Sayer and Knobelspiesse (2019).

## 3 Results

This section is divided into three main parts. Sect. 3.1 describes the geographical distribution of AOD and DOD trends, at global scale, by performing simultaneously a sensitivity analysis on: (i) the aggregation metric (geometric vs. arithmetic mean), (ii) the spatial resolution (fine vs. coarse), (iii) MIDAS trends evaluation (DOD vs. cAOD trends), and (iv) the applied temporal criteria (filters vs no filters). In Sect. 3.2, focus is given on the seasonal DOD trends whereas in Sect 3.3 emphasis is given on DOD trends at 12 regions of interest.

### 3.1 Global trends

### 3.1.1 Geometric vs. arithmetic mean

The overwhelming majority of the published AOD/DOD trend analysis studies have been relied on arithmetic mean in order to produce coarser spatial (e.g. 1° x 1°) and temporal (e.g. monthly values) resolutions. In this study, a sensitivity analysis on the aggregation method (i.e. arithmetic vs geometric mean), has been performed by utilizing the daily coarse spatial resolution (1° x 1°) MIDAS DODs. Figure 1 depicts the frequency histogram of MIDAS DODs in log scale using all the available data over the period 2003–2017. It is apparent that the shape of the DOD distribution is close to a log-normal distribution (Fig. 1). The latter considers the extreme dust episodes which force the distribution curve to be right-skewed. Arithmetic mean is about 4 times higher than the geometric mean, highlighting the importance of which metric is more representative of the population and how this can affect the results for specific applications (e.g. radiative forcing). When geometric standard deviation is considered, 65.43% of DOD values range between 0.002 and 0.027 while 81.04% encompassed within –0.033 and 0.099 for arithmetic mean, indicating an overstating of the variability (Sayer and Knobelspiesse, 2019). The averages and the standard deviations are calculated using weighted aggregation expressions with the weighting factors in terms of latitude (see Sect. 2.3). An additional point, revealing that the selection of normal statistics can lead to a misrepresentation of the population for a positive-definite quantity (i.e. dust optical depth), is that the lower bound (−0.033) is negative, which has not any physical meaning.

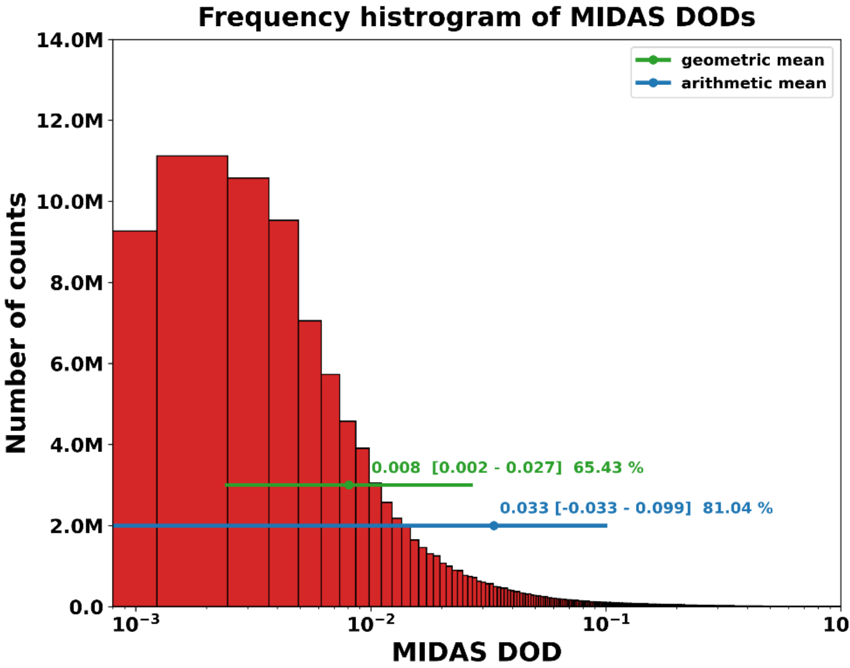

**Figure 1. Frequency histogram of MIDAS DODs reported at 1° x 1° spatial resolution over the period 2003 – 2017. The computed geometric mean (green) and arithmetic mean (blue) are given along with ranges corresponding to geometric mean/geometric standard deviation and geometric mean*geometric standard deviation for the geometric mean and ± standard deviation for the arithmetic mean.**

In agreement with Sayer and Knobelspiesse (2019), the calculated trends for AOD and DOD are consistent in terms of sign between fine (Fig. 2) and coarse (Fig. 3) spatial resolution data. However, in terms of magnitude this is not the case. Figure S1, S2 depicts the frequency histograms of the deviations between the arithmetic and geometric trends. When geometric AOD/DOD averages are considered, the deseasonalized trends are suppressed by up to 91.77% with the respect to the corresponding levels obtained from the arithmetic means, regardless the underlying surface type. The only exception is found for AOD at 1° spatial resolution and across oceanic territories (Fig. S2c) where geometric trends overestimate those of arithmetic by 71.63%.

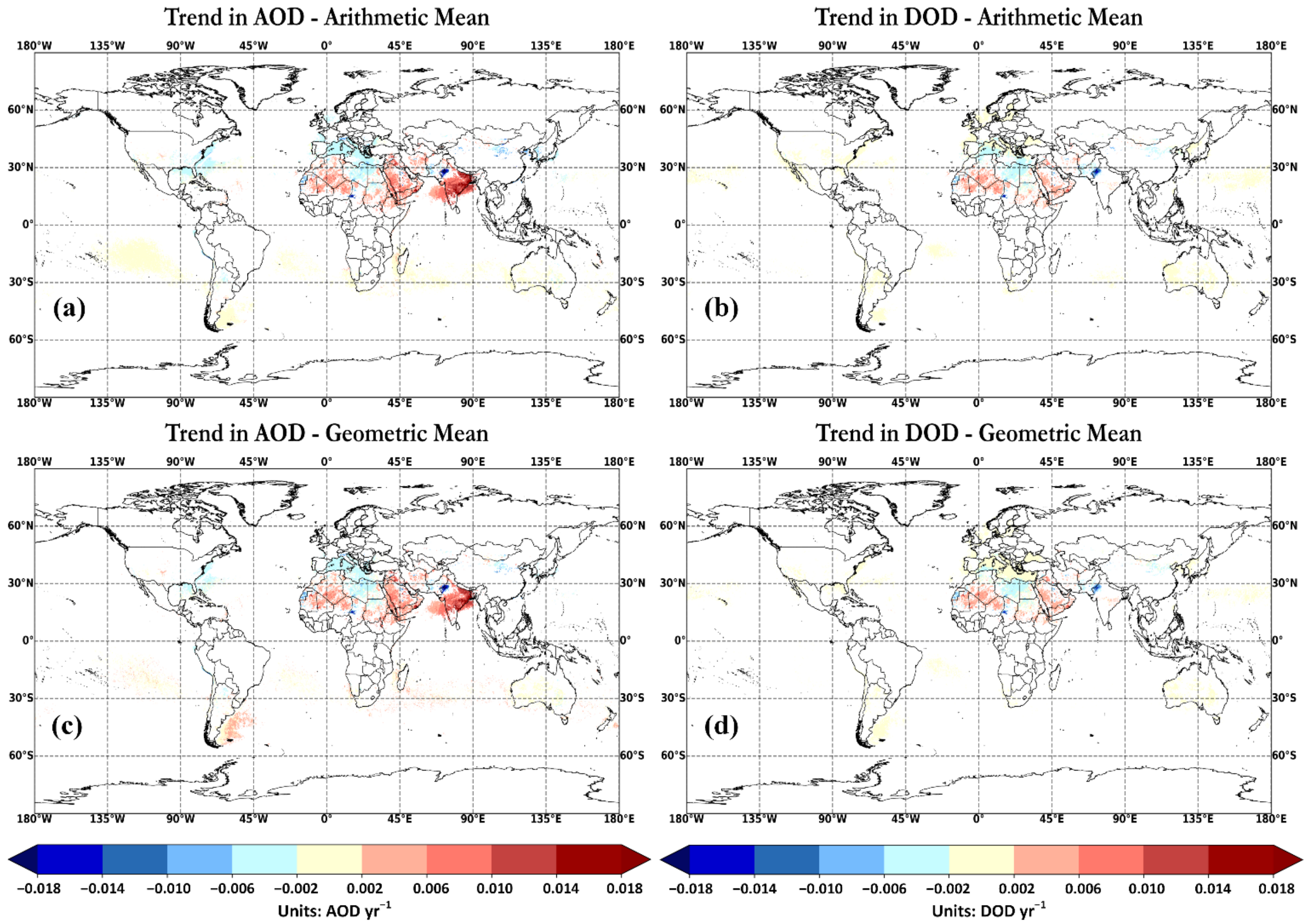

**Figure 2: Global maps of temporal trends (statistically significant at 95% confidence level), at 0.1° x 0.1° spatial resolution, calculated from the deseasonalized AOD (a and c) and DOD (b and d) monthly values during 2003 – 2017. Upper panel (a, b) shows the arithmetic-based trends while the bottom panel (c, d) indicates the geometric-based trends. The pixels with: 1) non-significant trends, 2) the temporal criteria are not met and 3) not available data are colored as white (blank) in each map of trend analysis. Neutral trends, ranging between −0.002 and 0.002 DOD yr$^{-1}$, are colored with light yellow (or cream) (the central color of the color bar). Figs S3a, S3b and S4 present the differences between the aforementioned colors at fine, coarse spatial resolution as well as for the easonal trends, respectively. Based on those Figs, the pixels with not available data are colored with gray color while those of failing to meet the availability criteria are colored with greenish.**

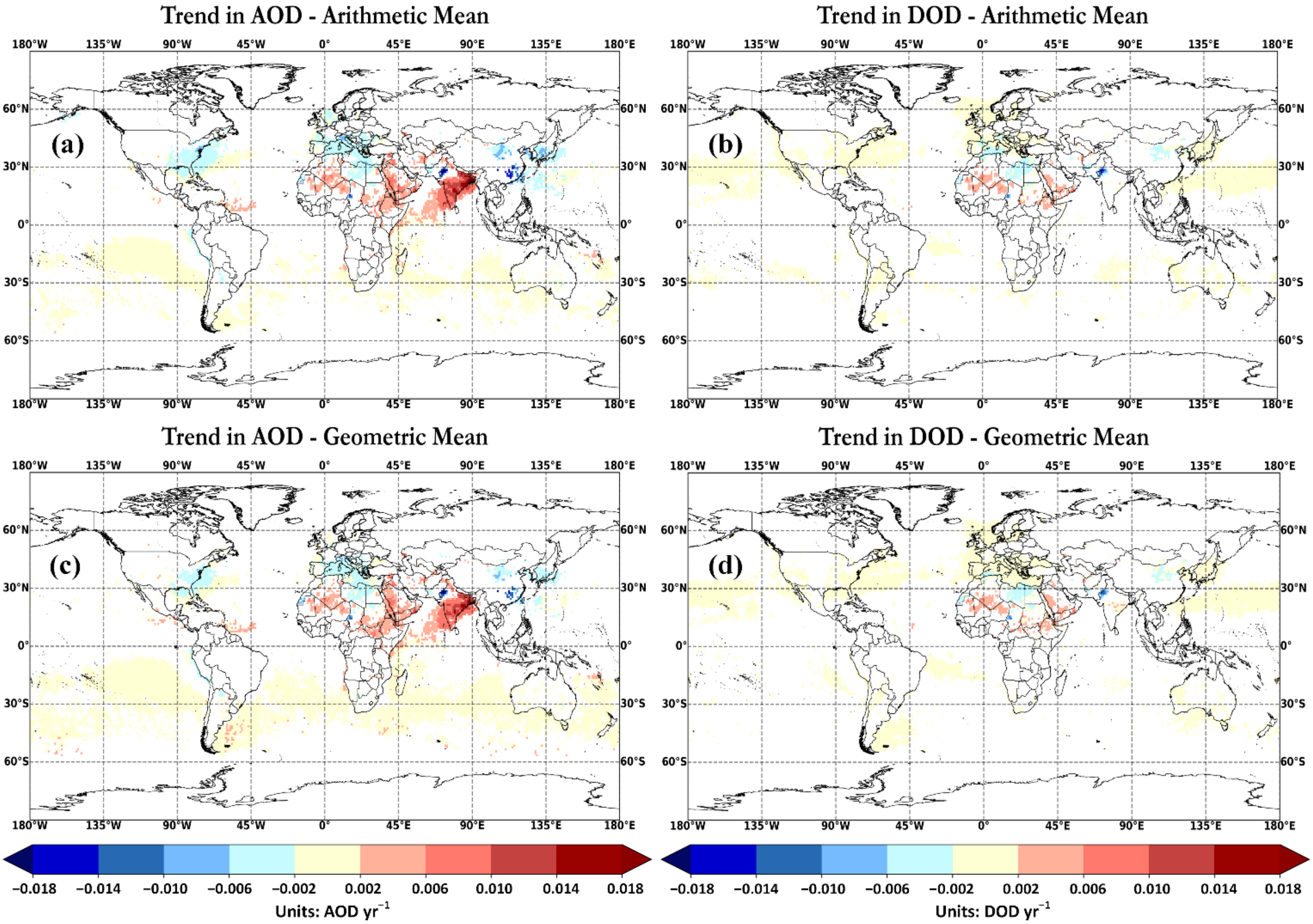

**Figure 3: Same as Fig. 2 at 1° x 1° spatial resolution.**

Across the dust-affected regions of the planet, the calculated AOD and DOD trends have revealed similar pattern. Over areas where the dust contribution to the total aerosol load is negligible, DOD trends are non-significant or neutral. For instance, strong positive AOD trends are depicted across India and the Bay of Bengal (Figs. 2a and 2c), whereas the recorded annual DOD tendencies are negligible (Figs. 2b and 2d). Similar findings are evident along the eastern coasts of US and in the Gulf of Mexico. In the Mediterranean Basin, engrossing disparities are recorded between AOD and DOD trends. Negative AOD trends are shown in the entire region with decreasing DOD trends confined in the southern areas near the North Africa coast (Figs. 2b and 2d). In addition, strong positive trends for AOD and DOD are revealed in Central Sahara (up to 0.026 $yr^{-1}$), across Mauritania-Algeria-Mali-Niger areas and the Arabian Peninsula. The highest positive tendencies are shown in Oman−Saudi Arabia borders (up to 0.031 $yr^{-1}$). On the contrary, decreasing AOD/DOD tendencies are observed in the Eastern (down to −0.017 $yr^{-1}$) and Western (down to −0.019 $yr^{-1}$) Sahara, in the Bodélé Depression of the Chad Basin (northern of Lake Chad), in the Gobi Desert (Northern China−Southern Mongolia) as well as in the Thar Desert (northwestern Indian subcontinent). Among the regions where declining tendencies are evident, the most negative ones are recorded in the Bodélé

Depression (down to −0.025 yr$^{-1}$) and in the Thar Desert (down to −0.029 yr$^{-1}$). A comprehensive regional analysis including the intercomparison with prior findings and the potential trends justification is discussed in Sect. 3.3.

### 3.1.2 Fine vs. coarse spatial resolution

The second sensitivity analysis aims to highlight differences of AOD/DOD trends when fine and coarse spatial resolution of MIDAS data are contrasted. De Meij et al. 2012 have investigated the differences between the fine daily MODIS AOD (L2; at 0.1° x 0.1° spatial resolution) and the coarse monthly MODIS AOD (L3; at 1° x 1° spatial resolution) in trend calculations utilizing the Collection 5 (C005) retrievals. According to their study, a good agreement was found between the L2 and L3 AOD trends over specific areas (i.e. Central Mediterranean, North-East America, and East Asia). At a first glance, the trend patterns reproduced by the fine (Fig. 2) and coarse (Fig. 3) MIDAS DODs are spatially consistent. Nevertheless, in terms of magnitude, the absolute values of DODs at coarser spatial resolution are lower in most of areas with evident signal (either positive or negative), such as the southern parts of the Arabian Peninsula (up to 0.014 yr$^{-1}$), the Bodélé Depression (down to −0.015 yr$^{-1}$) and the Thar Desert (down to −0.024 yr$^{-1}$). Coarser grid-cells in contrast to the finer spatial resolution meet the data availability threshold (≥ 60 months) (Fig. S3) defined for the calculation of temporal trends because of their more extensive spatial coverage. MIDAS meets adequately the temporal criteria (Sect. 2.2) both at fine (Fig. S3a) and coarse (Fig. S3b) spatial resolutions, providing grid cells of long-term AOD/DOD time series along with significant AOD (Figs. 2a, 2c, 3a and 3c) and DOD (Figs. 2b, 2d, 3b and 3d) tendencies. Trend analysis for the coarse grids yields a superior number of significant AOD tendencies globally (Figs. 3a and 3b). For instance, new and significant declining coarser AOD trends are observed in East Asia, particularly across Southeast Asia, the Yellow Sea, the Sea of Japan, and the North Pacific Ocean. Similarly, new increasing AOD trends are reported in the Southern Arabian Sea and the North Atlantic Ocean nearby the coast of Venezuela.

Voss and Evan (2020) generated two global DOD datasets using MODIS retrievals, combined with reanalysis data and AERONET inversion retrievals. They estimated the decadal DOD trends (see their Figs. 11a and 11b) based on MODIS/Terra (2001−2018) and MODIS/Aqua (2003−2018) data projected at an equal lat-lon 1° spatial resolution. In order to compare the findings in this study against Voss and Evan (2000), only arithmetic DOD trends are used at the same grid-cell spatial resolution (Fig. 3b). In addition, since MIDAS dataset relies on MODIS-Aqua retrievals (Sect. 2.1), only their DOD MODIS/Aqua dataset is used for comparison. Table 1 displays the ranges of DOD trends between the two datasets over 15 desert and downwind areas of the globe. The selection of the above regions is accomplished based on the areas in which statistically significant DOD trends are revealed in Voss and Evan (2020) study. Over the Sahara Desert, Bodélé Depression and Thar desert, identical significant trends in terms of magnitude and sign are recorded in both studies. Over Arabian Peninsula, the calculated trends here are common in terms of sign but lower in terms of magnitude. More specifically, the current study reports declining DOD trends along the Mediterranean Basin, while Voss and Evan (2020) did not find any significant trends. On the other side, they reported strong positive trends over Tropical Atlantic Ocean, sub-Sahel, Northeast Middle East and Northeast Caspian and

Aral Sea which is not the case here. Trend inconsistencies are revealed because of a) the derivation algorithm of DOD, b) the trend detection methodology, c) the different study periods, and d) the temporal filtering criteria.

**Table 1: Comparison of the computed DOD trends between the current study and the Voss and Evan (2020) over 15 regions of interest.**

| Regions | Latitude (°) | Longitude (°) | Current study (DOD yr$^{-1}$) | Voss and Evan (2020) (DOD yr$^{-1}$) |
|---|---|---|---|---|
| **Desert areas** | | | | |
| West Sahara | 21 – 26 N | 12 – 16 W | –0.010 - – 0.002 | –0.010 - –0.002 |
| Central Sahara | 15 – 30 N | 10 W – 15 E | 0.002 - 0.010 | 0.002 - 0.010 |
| East Sahara | 18 – 30 N | 15 – 30 E | –0.006 - – 0.002 | –0.006 - – 0.002 |
| Bodélé Depression | 13 – 16 N | 12 – 18 E | –0.018 - – 0.002 | –0.018 - – 0.002 |
| Middle East | 10 – 35 N | 35 – 50 E | 0.002 - 0.018 | 0.002 - 0.021 |
| Thar Desert | 24 – 30 N | 68 – 76 E | –0.018 - – 0.002 | –0.021 - – 0.002 |
| Gobi Desert | 37 – 45 N | 90 – 110 E | –0.006 - – 0.002 | –0.010 - – 0.002 |
| **Downwind areas** | | | | |
| Sub-Sahel | 0 – 13 N | 60 W – 20 E | Non-significant | 0.002-0.018 |
| Mediterranean Basin | 30 – 45 N | 10 W – 30 E | –0.006 - – 0.002 | –0.002 - 0.002 |
| Region surround Caspian Sea | 35 – 60 N | 45 – 60 E | Non-significant | 0.002 - 0.021 |
| Tropical Atlantic Ocean | 0 – 15 N | 20 – 60 W | Non-significant | 0.002 - 0.006 |
| South Atlantic Ocean | 30 S – 0 | 13 W – 13 E | Non-significant | –0.006 - 0.006 |
| North Pacific Ocean | 40 – 60 N | 140 E – 120 W | Non-significant | –0.010 - – 0.010 |
| North Pacific and North America | 15 – 40 N | 140 E – 75 W | –0.002 - 0.002 | –0.002 - 0.002 |
| South Pacific Ocean | 45 – 15 N | 160 E – 80 W | –0.002 - 0.002 | –0.002 - 0.002 |

### 3.1.3 Evaluation of MIDAS trends vs. AERONET

The validity of the computed MIDAS DOD trends is thoroughly analyzed in this section. For evaluation purposes, the coarse mode AOD, hereafter referred as cAOD, retrieved through the AERONET SDA algorithm is applied. The two datasets are collocated by spatially averaging MIDAS DODs included in an area of 3x3 pixels around each AERONET site, and also temporally combined using solely the same daily values. DOD and cAOD trends are calculated using the methodology described in Sect. 2.3. Figure 4a illustrates the geographical distribution of the AERONET stations (in total 41) satisfying the defined temporal criteria (see Sect. 2.3) and finally used in the assessment analysis. According to Fig. 4b, a good linear correlation (R = 0.86) of the derived trends is observed accompanied with low bias (MBE = $-0.04x10^{-2}$). In order quantify the performance of MIDAS in capturing the cAOD trends, the total accuracy (TA) of the correct trends (identical sign) is calculated. More specifically, TA is defined as the percentage of the stations with correct trends sign (the sum of B1 and A2 quadrants numbers in Fig. 4c divided by the total number of stations). MIDAS trends can capture the correct cAOD trends signs with a TA of 80.5% (Fig. 4c). In addition, the percentages of each quadrant in Fig. 4c shows the number of the correctly detected stations per sign. The overwhelming majority of the AERONET stations encompassed negative trends (30 out of 41 stations). MIDAS trends capture the 26 out of those 30 (86.7%) stations denoted with negative cAOD trends. Lastly, there are only 11 sites with positive cAOD trends, and MIDAS proved able to detect them at 7 out of 11 (63.6%) stations.

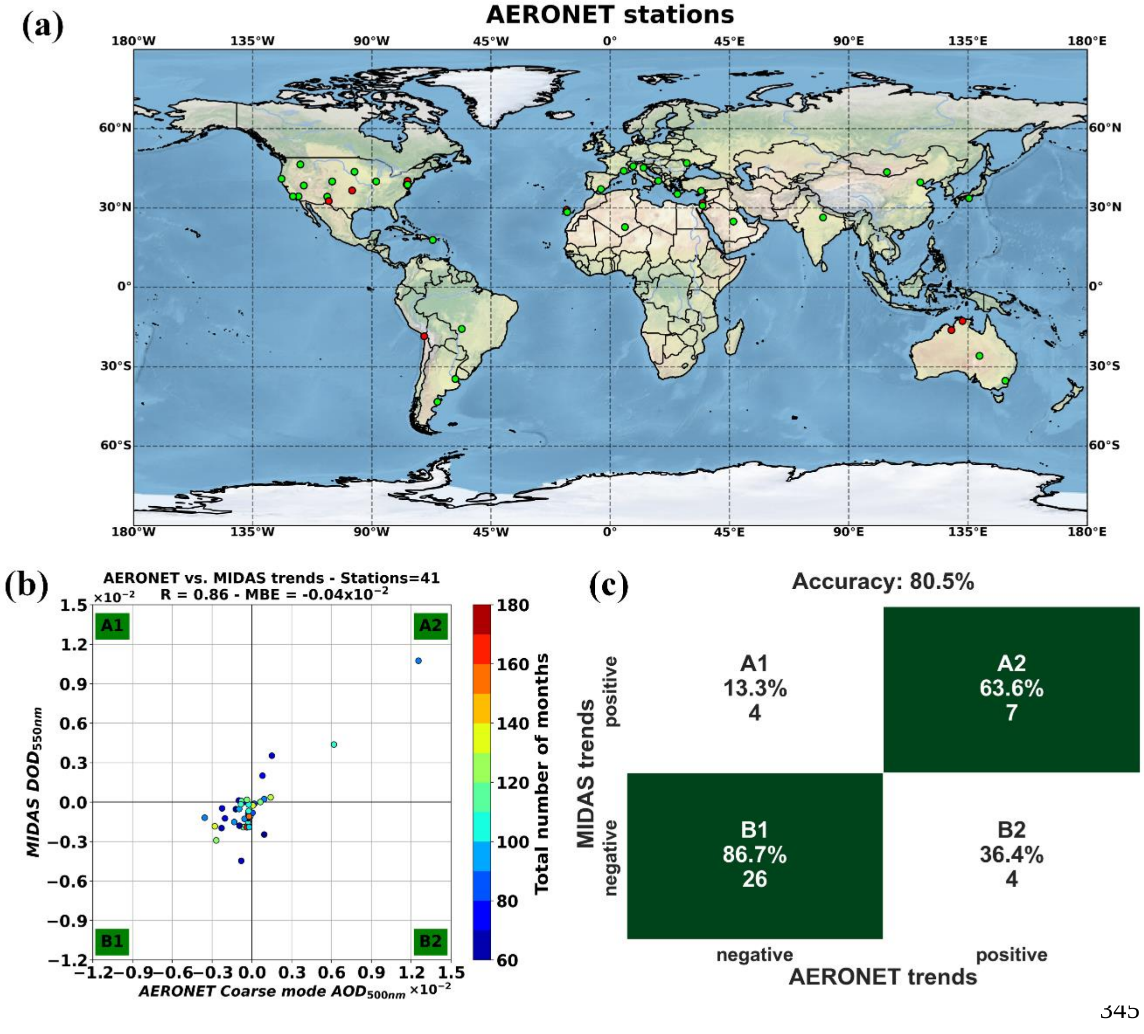

**Figure 4: (a) Geographical location of the available AERONET stations in which the temporal trends of DOD and cAOD are calculated. Green and red dots refer the stations with the similar and different trend sign, respectively. (b) Scatter plot between MIDAS DOD and AERONET cAOD trends. The color bar indicates the total number of months. (c) Confusion matrix of possible trend signs among the two datasets.**

Table S1 provides the point-to-point trend results for each collocated MIDAS-AERONET sites. It should be mentioned that among the revealed stations, few indicate dust particles as the predominant aerosol type. Based on Logothetis et al. (2020), the station of Solar Village, Arabian Peninsula, is primarily a "dusty" site revealing significantly high percentages of coarse absorbing particles. Across this station, the trends between AERONET cAOD (0.0126 $yr^{-1}$) and MIDAS DOD (0.0107 $yr^{-1}$) are in good agreement in terms of magnitude, but both are non-significant at the 95% confidence level. Similar findings are also observed in the "dusty" site of Tamanrasset, Algeria, showing increasing cAOD and DOD trends of 0.0062 $yr^{-1}$ and 0.0044 $yr^{-1}$, respectively. One of the advantages of MIDAS is that it provides the dust aerosols burden information in downwind regions of the planet. For instance, most of the stations located in South Europe receive dust particles transported towards the Mediterranean from Sahara and Middle East deserts, encompassing identical trend signs (Fig. 4a). Moreover, there are many downwind regions across different regions of the globe with similar trends magnitude such as Ispra, Italy (cAOD= –0.0013 $yr^{-1}$, DOD= –0.0015 $yr^{-1}$), Kanpur, India (cAOD= –0.0027 $yr^{-1}$, DOD= –0.0029 $yr^{-1}$), SERC (cAOD= –0.0023 $yr^{-1}$, DOD= –0.0020 $yr^{-1}$) in US, Shirahama, Japan (cAOD= –0.0020 $yr^{-1}$, DOD= –0.0012 $yr^{-1}$), and XiangHe, China (cAOD= –0.0028 $yr^{-1}$, DOD= –0.0018 $yr^{-1}$).

### 3.1.4 Filtering vs. non-filtering trends

The third sensitivity analysis of this section concerns the calculation of temporal trends using filtered (Fig. 2) and non-filtered (Fig. 5) data at fine spatial resolution. Here, the AOD/DOD trends are calculated by applying two consecutive temporal filters (Sect. 2.3). More specifically, the two applied temporal filters include the: 1) the calculation of the monthly averages when at least 6 days are available and 2) the trend calculation only in grid cells with higher than 60 available months (5 years). The total number of grid points for trend calculation increases when the above two temporal filters are not applied. Overall, months with more than one daily measurement are retained for trend analysis, increasing the total data availability of the entire global grid from 36% (filtered) to 83% (non-filtered).

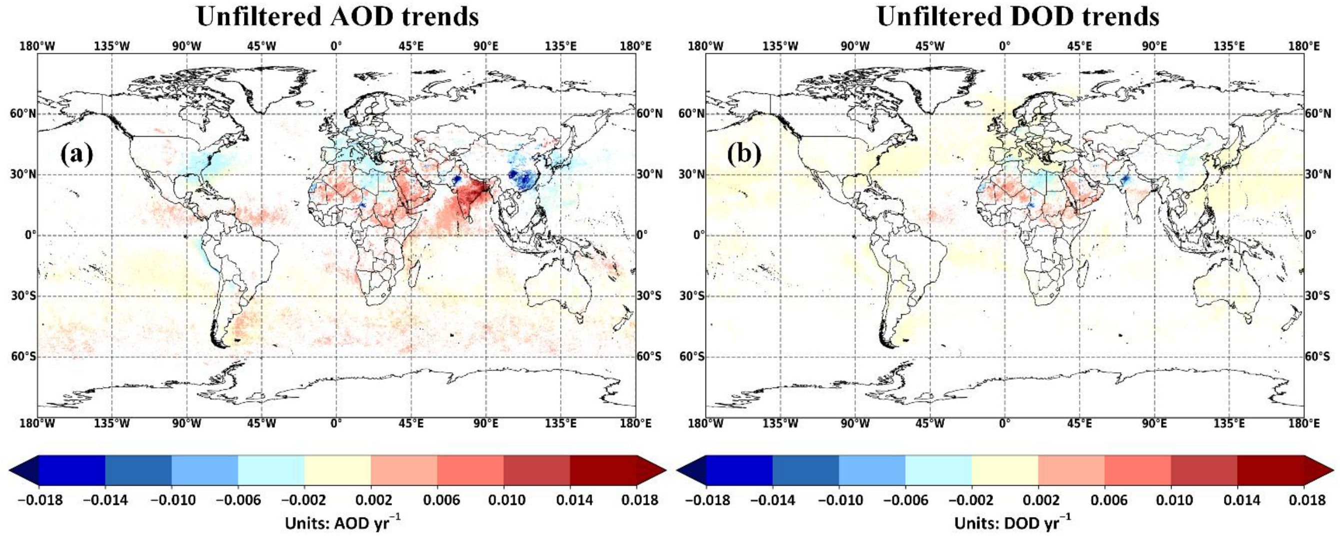

**Figure 5: Global maps of unfiltered temporal trends (statistically significant at 95% confidence level), at 0.1° x 0.1° spatial resolution, calculated from the deseasonalized geometric (a) AOD and (b) DOD monthly values during 2003 – 2017**.

According to Eq. (3), $\sigma_\omega$ (Fig. S5) and the statistical significance (Fig. S6) of the trend are controlled by $\sigma_N$, $\varphi$ (Fig. S7) and n (Fig S3). The differences in data availability between the unfiltered and filtered trend analysis are depicted in Fig. S8. Across the desert areas, the number of filtered months is adequately high and very close to the non-filtered case (Fig. S8). Thus, no trend differences in magnitude and sign are recorded. Over maritime and continental dust affected areas, new statistically significant AOD and DOD trends are represented when the unfiltered data are employed. Firstly, the number of pixels with statistically significant DOD trends has been significantly increased (Fig. 5b) but the majority of the new trends are mainly neutral located over oceanic territories (yellow pixels). New positive DOD tendencies are observed over Tropical Atlantic and India while new negative trends are recorded across Southeast China (Fig. 5b). Secondly, the significant AOD trends grid points are also strongly increased. New decreasing AOD trends are observed over USA, China and Philippine Sea (Fig. 5a). Especially across the region of southeastern China, the number of significant AOD trends has been increased profoundly. In addition, new AOD increasing trends are recorded over Tropical Atlantic, North Pacific (West of Mexico), Arabian Sea and the oceanic area between 30.0°S and 60.0°S. Despite the increase in monthly data availability, trend analysis without temporal filtering may lead to erroneous and not representative results either for AOD or DOD. In order to investigate in detail the last statement, a sensitivity analysis is performed using in total 76 AERONET stations (Fig. S9a). Through the evaluation analysis of MIDAS DOD trends (Sect. 3.1.3), the AERONET stations have been selected based on their data availability. More specifically, only the stations with at least 10 years of data have been retained for further analysis. Tahe total number of sites has been decreased from 76 (here) to 41 due to temporal filtering (see Sect. 3.1.3). Based on Fig. S9b, the unfiltered temporal trends between MIDAS and AERONET documented a profoundly lower linear correlation (R=0.51) while the data points are more sparse. When trends are calculated without any temporal filtering, the total accuracy of the correct trends has been decreased from 80.5% (Fig. 4c) to 73.7% (Fig. S9c).

In the following sections, and considering all three implemented sensitivity analysis, only the geometric-based DOD and AOD trends (Sect. 3.1.1) at fine spatial resolution (Sect. 3.1.2) including the temporal filtering (Sect. 3.1.4) are discussed.

### 3.2 Seasonal trends

Dust aerosols' burden is subjected to strong intra-annual and interannual variations with different cycles depending on the source or downwind region (Gkikas et al., 2021b). Here, the seasonal DOD tendencies at a global scale (Fig. 6) are calculated based on the methodology proposed by Hsu et al. (2012). The corresponding seasonal AOD trends are depicted in Fig. S10.

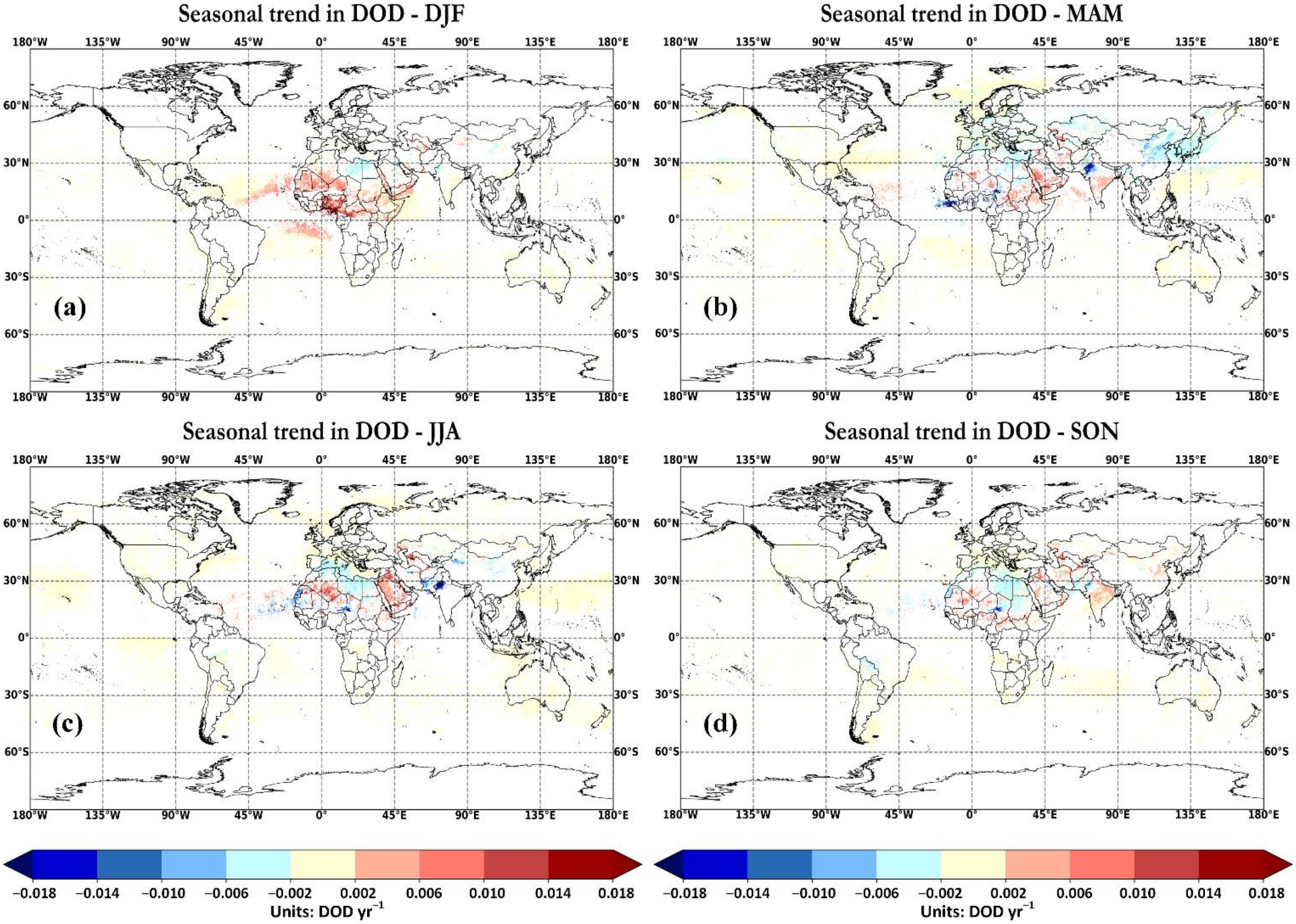

**Figure 6: Seasonal geographical distributions of DOD temporal trends at (a) December-January-February (DJF), (b) March-April-May (MAM), (c) June-July-August (JJA) and (d) September-October-November (SON).**

The detection of the statistical significance of the calculated trends based on Weatherhead et al. (1998) cannot be applied here due to the 9-month gap among the seasons. Therefore, an alternative approach is followed by calculating the seasonal trends using a simple linear regression model on the DOD anomalies and identifying the statistically significant trends based on the two-sided Student's t-test. The null hypothesis of the t-test assumes a non-significant temporal trend under a defined confidence level (here is 95%). The total number of months for each season is displayed in Fig. S4. Only the grid points with more than 13 available months (13 from 45 total months) are retained. The performed analysis at global scale and on a seasonal basis highlights many regions with significant DOD trends (Figs. 2 and 6) which are used to define regional domains (Fig. 7).

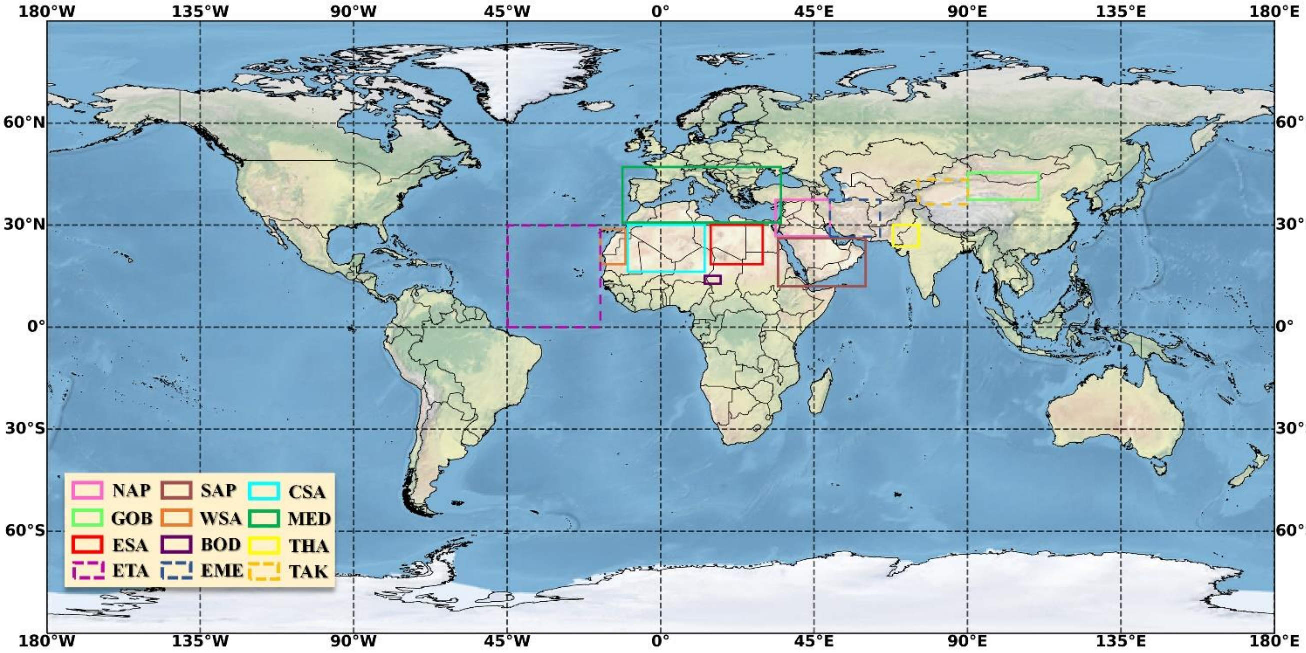

**Figure 7: Regions of interest for seasonal and regional analysis: North Arabian Peninsula (NAP), South Arabian Peninsula (SAP), Central Sahara (CSA), Gobi Desert (GOB), West Sahara (WSA), Mediterranean (MED), East Sahara (ESA), Bodélé Depression (BOD), Thar Desert (THA), East Tropical Atlantic (ETA), Eastern Middle East (EME) and Taklamakan Desert (TAK). Solid rectangles indicate the regions which are included in the regional analysis (Sect. 3.3) while solid and dashed rectangles are for the seasonal analysis.**

The Sahara Desert, hosting some of the most active aeolian natural dust sources of the planet, is a region of great interest for investigating the intra-seasonal DOD variations. In its central sector, increasing trends are recorded throughout the year (maximum positive value in JJA) (Table 2). On the contrary, negative seasonal DOD trends appear in the majority regions across North Africa (Fig. 6). The western and eastern parts of the Sahara Desert present strong declining trends maximized during boreal summer (Table 2). From spring to autumn, in the Bodélé Depression, substantial decreasing trends are recorded (Table 2). Over the period 2001−2012, dust emissions in the broader area of the Bodélé Depression were decreased in summertime, which was attributed to the increased rainfall, caused by the positive trends of the Sahara heat lows (SHL), the warm phase of Atlantic Multi-decadal Oscillation (AMO) and the decreasing trends in terms of occurrence and intensity of nocturnal low-level jets' (NLLJ) (Shi et al., 2021). Surface wind speed also affects dust emissions across North Africa (Evan et al., 2016). Surface wind speed and NLLJ are the principal drivers for the interannual variation of dust emissions across Western Sahara, while in summertime dust emissions decreased during 2001−2012 (Shi et al., 2021). The eastern sector of North Africa (North Libya and Egypt) presents moderate negative trends maximized in winter (down to −0.014 yr$^{-1}$) and spring (down to −0.011 yr$^{-1}$). In the western sector (i.e. north Algeria and Tunisia) strong significant declining trends are observed in summer (down to −0.035 yr$^{-1}$) (Fig. 6c). The dust sources residing near the North African coasts are strongly influenced by the surface wind speed, NLLJ, Harmattan surge and the tracks of the Mediterranean depressions (Shi et al., 2021).

**Table 2: Seasonal trends over 12 regions of interest. Each column includes: the range of DOD trend (yr$^{-1}$) and the median DOD trend. Non-available values are shown in blank cells. The domains of the regions are depicted in Fig. 7.**

| Region | Winter (DJF) | Spring (MAM) | Summer (JJA) | Autumn (SON) |
|---|---|---|---|---|
| **Central Sahara Desert** | −0.007-0.017, 0.004 | −0.025-0.027, 0.007 | −0.018-0.031, 0.007 | −0.014-0.019, 0.005 |
| **Western Sahara Desert** | −0.009-0.013, 0.004 | −0.021-0.022, −0.006 | −0.028-0.017, −0.008 | −0.016-0.009, −0.004 |
| **Eastern Sahara Desert** | −0.011-0.007, −0.003 | −0.017-0.013, −0.004 | −0.020-0.012, −0.003 | −0.014-0.006, −0.003 |
| **Bodélé Depression** |  | −0.038-0.015, −0.014 | −0.025-0.014, −0.011 | −0.028-0.011, −0.011 |
| **North Arabian Peninsula** | −0.011-0.005, −0.003 | −0.016-0.026, −0.003 | −0.019-0.026, 0.005 | −0.010-0.016, 0.004 |
| **South Arabian Peninsula** | −0.013-0.012, 0.002 | −0.019-0.026, 0.006 | −0.020-0.024, 0.006 | −0.016-0.013, 0.003 |
| **East Middle East** | −0.011-0.007, 0.002, | −0.022-0.020, 0.004 | −0.032-0.016, −0.005 | −0.025-0.013, 0.002 |
| **East Tropical Atlantic** | −0.010-0.022, 0.003 | −0.022-0.022, −0.002 | −0.029-0.019, 0.00 | −0.012-0.014, −0.002 |
| **Mediterranean** | −0.014-0.009, −0.001 | −0.032-0.009, −0.002 | −0.035-0.011, −0.002 | −0.015-0.004, −0.002 |
| **Thar Desert** | −0.007-0.002, −0.004 | −0.024-0.004, −0.012 | −0.047-−0.001, −0.021 | −0.013-0.003, −0.005 |
| **Taklamakan Desert** | −0.005-0.010, −0.003 |  | −0.027-0.019, −0.006 |  |
| **Gobi Desert** | −0.010-0.006, −0.002 | −0.023-0.014, −0.005 | −0.011-0.005, −0.002 | −0.005-0.012, 0.001 |

Numerous studies have notified the Saharan transatlantic transport (Peyridieu et al., 2013; Alizadeh-Choobari et al., 2014c; Prospero et al., 2014; Gläser et al., 2015; Fréville et al., 2020; Gkikas et al., 2021b). Across the Gulf of Guinea and mid-Atlantic, relatively high DODs are documented in boreal winter, ranging from 0.1 to 0.2 (up to 0.6) (Gkikas et al., 2021b). According to Fig. 6a, strong positive DOD trends are shown over Gulf of Guinea (up to 0.047 yr$^{-1}$). In this season, strong northeasterly winds (Harmattan) transport intense loads of Saharan dust towards Nigeria and the Gulf of Guinea (Washington et al., 2006). However, the trend magnitude along the Gulf of Guinea as well as in the northern regions (from Ghana to Cameroon) seems to be unreliable due to the reduced performance of MDF, surface contamination in the received radiances by MODIS and to the co-existence of aerosols and clouds (Gkikas et al., 2021b). In order to investigate the reliability of MIDAS DOD in the above region, the seasonal trend analysis is implemented at the AERONET station of llorin, Nigeria. It worths mentioning that this station has not been included in evaluation analysis of Sect. 3.1.3, due to the low number of months ($N=48<60$). However, 32 out of 48 months lie in boreal winter, enabling the application of the methodology during this season. Both datasets represented increasing and statistically significant cAOD (0.011 yr$^{-1}$, $|\omega/\sigma_{\omega}|=2.43$) and DOD trends (0.021 yr$^{-1}$,

$|\omega/\sigma_\omega|=3.74$). As expected, MIDAS revealed higher in magnitude trends than cAOD (approximately 2 times higher). In the case of AOD (Fig. S10a), identical positive trends as DOD are shown in winter. Interestingly, substantial negative DOD trends (down to −0.045 $yr^{-1}$) are recorded during springtime in an area among Guinea, Sierra Leone and North Atlantic Ocean (Fig. 6b), while positive tendencies are documented over Tropical Atlantic Ocean in DJF (Table 2). Over the region extended from the North Atlantic Ocean to the Eastern Caribbean Sea (Lat: 10.0 ºN−18.0ºN; Lon: 70.0 ºW−45.0 ºW), moderate positive trends are documented predominantly in MAM (up to 0.010 $yr^{-1}$) and JJA (up to 0.008 $yr^{-1}$). Dust transport from North Africa along the Atlantic Ocean reaches the Caribbean Sea, while summer DODs are intertwined with tropical Atlantic cyclone activity. More specifically, Caribbean DOD during summer is negatively correlated to Atlantic accumulated cyclone energy and Atlantic Meridional Mode index (Xian et al., 2020). In addition, dust aerosol burden originated form Sahara Desert is directly related to tropical cyclones (TCS) over Tropical Atlantic Ocean, but their relationship is not unambiguously clarified (Evan et al., 2006). Based on model simulations, Pan et al. (2018) investigated the role of dust aerosols for the genesis of TCs over tropical Atlantic basin, by comparison of dust and non-dust model simulations. They revealed that dust amount is directly related to TCs, revealing a bimodal pattern. More specifically, favorable conditions for TCs formation are documented by increasing the midlevel moisture and decreasing the vertical wind shear while unfavorable conditions are encompassed by decreasing the low-level vorticity and potential intensity.

Increasing tendencies, throughout the year, appear in the Middle East (Table 2), with few exceptions, particularly in the northern Arabian Peninsula (Fig. 6). More specifically, the southwestern sector of Oman presents the highest increasing trends for all seasons (up to 0.026 $yr^{-1}$). Similarly, high positive trends in MAM (up to 0.015 $yr^{-1}$) and JJA (up to 0.018 $yr^{-1}$) are documented over the western part of Saudi Arabia. Negative tendencies are observed for all seasons at the north of the Oroug Bani M’aradh Wildfire Sanctuary (South Saudi Arabia) including strongly negative DOD trends in summer (down to −0.020 $yr^{-1}$) and spring (down to −0.019 $yr^{-1}$). In the northern part of the Arabian Peninsula, positive trends are detected predominantly in JJA and SON. Dust activity across the Arabian Peninsula is strongly influenced by the intensity of the northwesterly Shamal winds, favored by the low precipitation amounts during summer (Yu et al., 2015). The temporally extended drought (Notaro et al., 2015) along with the cooling of the Tropical Indian Ocean and the Mediterranean Sea temperatures (Yu et al., 2015), leading to an enhancement of the Shamal winds, could regulate the summer DOD trends across Arabian Peninsula. During springtime, La Niña events constitute the principal drivers for the dust activity by reducing the rainfall amounts over Rub’ al Khali Desert; one of the most active dust sources across the Arabian Peninsula (Yu et al., 2015). Strong positive trends (up to 0.026 $yr^{-1}$) are encountered in MAM and JJA over Iraq, while significant increasing trends are recorded for all seasons across the eastern Iran, with the most evident ones in spring (up to 0.020 $yr^{-1}$). However, a hotspot of strong declining trends exists in southeastern area of Iran (34.5°N, 54.5°E) with the most negative values in JJA (down to −0.029 $yr^{-1}$) and SON (down to −0.025 $yr^{-1}$). Moderate negative DOD trends are documented during the summertime (down to −0.01 $yr^{-1}$) across the Alboran Sea (western Mediterranean). The dust aerosol burden has also been decreased in the eastern part of Mediterranean Sea during spring (down to −0.006 $yr^{-1}$, from Lybia and Egyptian coasts to Aegean Sea) and autumn (down to −0.005 $yr^{-1}$, across the Gulf of Sidra).

Statistically significant positive DOD trends are detected across the intersection of Kazakhstan, Uzbekistan and Turkmenistan, in the northeastern Caspian Sea shore. At all seasons, the DOD trends exceed 0.011 $yr^{-1}$ while the maximum trends are recorded in summer (up to 0.035 $yr^{-1}$) and spring (up to 0.019 $yr^{-1}$). These findings substantiate the positive decadal DOD trends (~0.18 $decade^{-1}$) of Voss and Evan (2020) and could be attributed to the amount of drawdown (~−6.72 cm $yr^{-1}$) in the Caspian Sea level during 1996−2015 (Chen et al., 2017). Central, South and East Asia constitute another regions of interest in which robust DOD trends are encountered (Fig. 6). The maximum negative values are depicted over the Thar Desert in JJA and MAM (Table 2). It must be highlighted that the maximum decreasing trends are detected during the high-dust season in the Thar Desert (Proestakis et al., 2018). The reduction of dust load during the pre-monsoon (MAM) could be attributed to the increase of the rainfall and soil moisture levels, acting in favor of wet dust deposition as well as decreasing the dust erosion (Pandey et al., 2017; Jin and Wang, 2018; Lakshmi et al., 2019). Moreover, reductions in dust emissions are recorded during summertime, which are strongly linked to soil moisture and wind speed (Shi et al., 2021). In Northwest China (Central Asia) lies the Taklamakan Desert, where non-significant annual trends are documented (Fig. 2). However, significant seasonally negative DOD trends are observed (Fig. 6) particularly in summertime (Table 2). Additionally, over the Gobi Desert and East Asia strongly negative DOD tendencies are documented mainly in spring (Fig. 6b), when the dust activity peaks (Proestakis et al., 2018). The negative DOD trends across the Gobi Desert could be attributed to reduced dust emissions, caused by the decrease of surface wind speed which has been recorded between 2010−2016 (Guo et al., 2019).

### 3.3 Regional trends

The regional DOD and AOD trends are calculated for 9 specific regions of interest (Table 3 and Fig. 7 solid rectangles) as well as for the whole globe (GLB) and separately over land (GLB-L) and ocean (GLB-O) (Sect. 3.3.1). The full names of each region as well as the calculated regional DOD trends and their uncertainties are included in Table 3. The comparisons among the geometric vs. arithmetic aggregation method and coarse vs. fine spatial resolution are also investigated for the regional DOD (Fig. 8a) and AOD (Fig. 8b) trends. On a regional basis, the temporal trends between the two spatial resolutions are in very good agreement, corroborating de Meij et al. (2012). Since the statistical significance of the trends is strongly influenced by the number of years and the study period, the regional DOD trends are also computed for different time periods considering the systematic change of time period (number of years) and initial year (Fig. 9).

**Table 3: Global and regional temporal DOD trends based on MIDAS dataset. The trends with the ratio $|\omega/\sigma_{\omega}|$ higher than 2.0 are statistically significance at 95% confidence level. The star symbol corresponds to statistically significant regions under the 95% confidence level. The domains of the regions are represented in Fig 7.**

| Region | Acronym | Trend (ω, DOD yr$^{-1}$) × 10$^{-3}$ | Uncertainty ($\sigma_{\omega}$) × 10$^{-3}$ | $|\omega/\sigma_{\omega}|$ |
|---|---|---|---|---|
| **lobal land & ocean** | **GLB** | 0.022 | 0.12 | 0.19 |
| **Global land** | **GLB-L** | 0.082 | 0.25 | 0.33 |
| **Global ocean** | **GLB-O** | −0.017 | 0.069 | 0.24 |
| **North Arabian Peninsula** | **NAP** | 0.60 | 1.3 | 0.45 |
| **South Arabian Peninsula** | **SAP** | 1.80 | 1.2 | 1.5 |
| **Central Sahara** | **CSA** | 2.1 | 0.87 | 2.4$^{*}$ |
| **Gobi Desert** | **GOB** | −0.71 | 0.39 | 1.8 |
| **West Sahara** | **WSA** | −0.95 | 0.85 | 1.1 |
| **Mediterranean** | **MED** | −1.1 | 0.30 | 3.8$^{*}$ |
| **East Sahara** | **ESA** | −1.8 | 0.61 | 3.0$^{*}$ |
| **Bodélé Depression** | **BOD** | −5.5 | 2.6 | 2.1$^{*}$ |
| **Thar Desert** | **THA** | −5.3 | 1.9 | 2.8$^{*}$ |

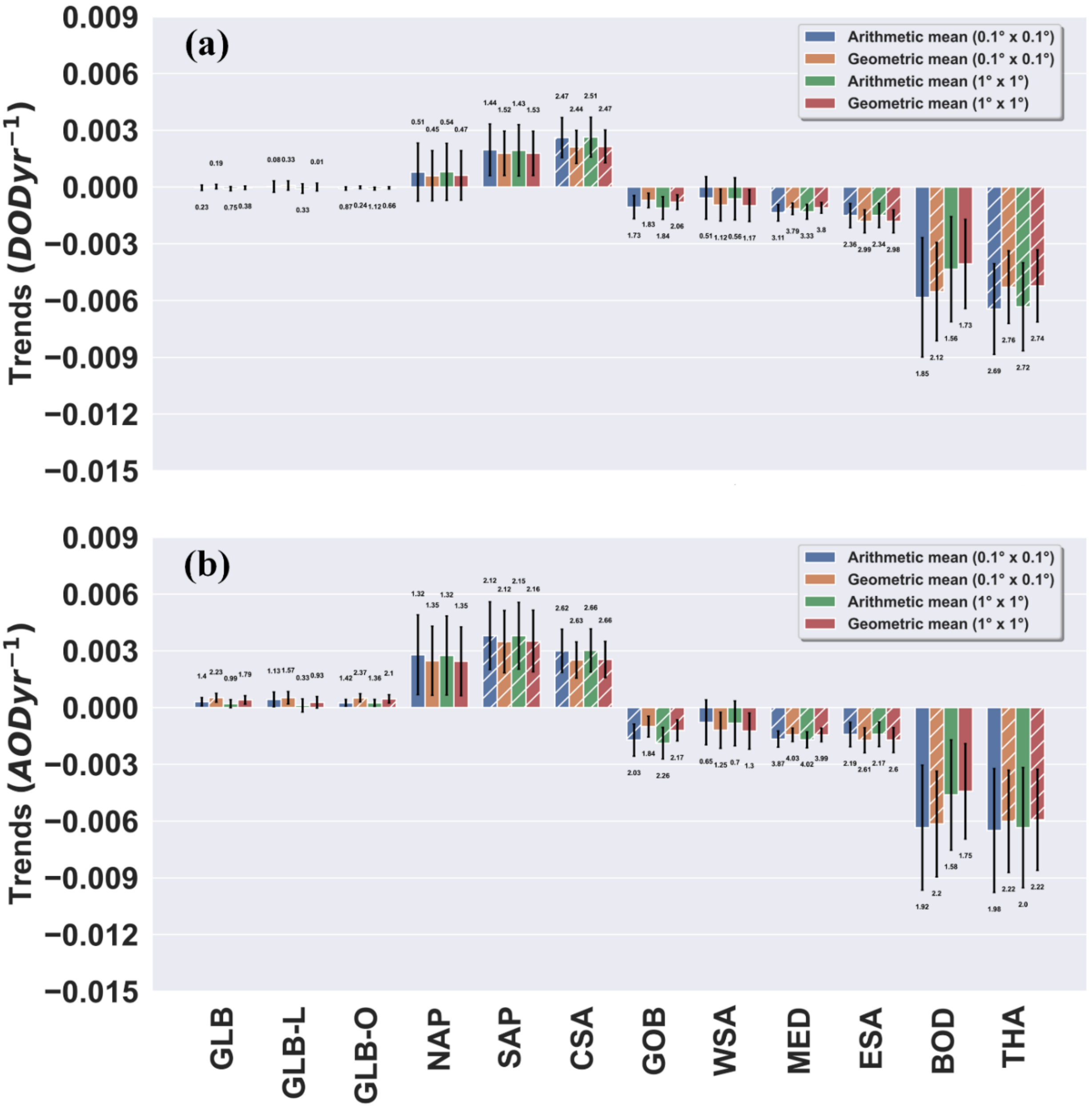

**Figure 8: Bar-plots indicating the (a) DOD and (b) AOD regional temporal trends. The hatched bars represent regions with the significant trends ($|\omega/\sigma_\omega| > 2.0$). The error bars denote the uncertainty of the trends based on Eq. (3) (Sect. 2.3).**

The explanation of the temporal evolution of calculated trends shown in Fig. 9 is presented in the next section for individual regions.

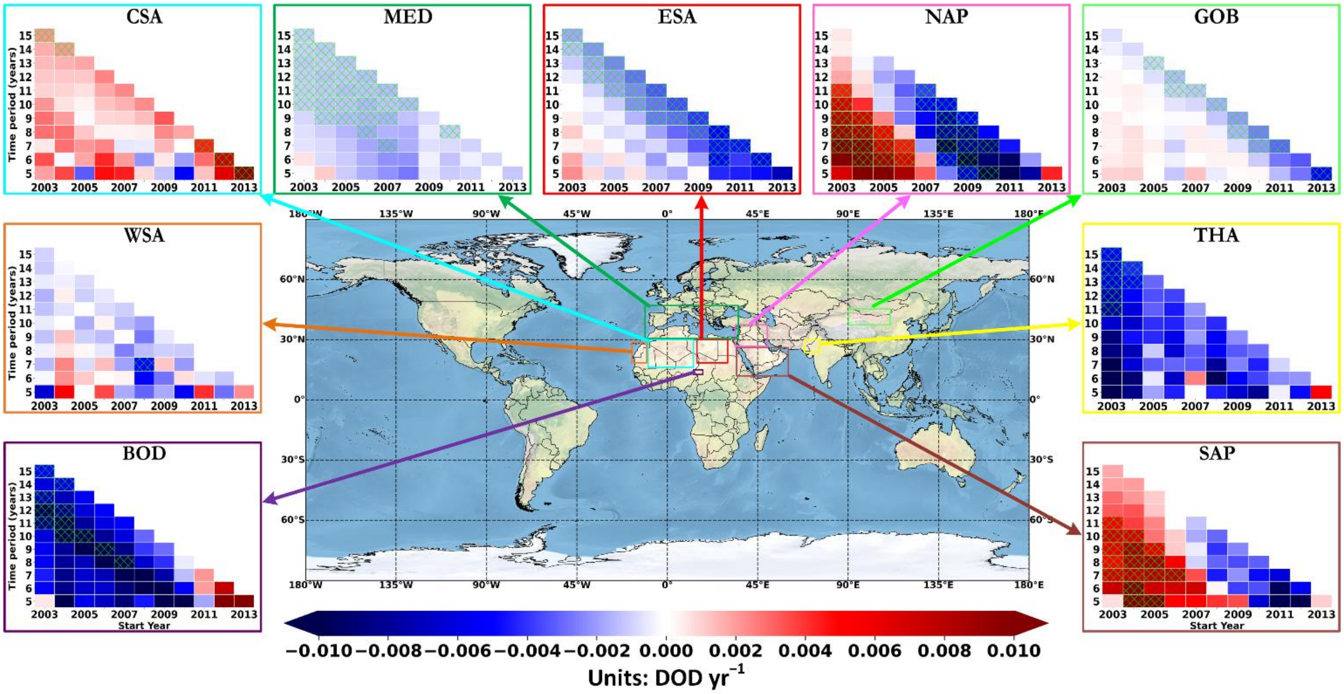

**Figure 9: Regional DOD trends at different time intervals, with at least 5-year time series. The acronyms full names are documented in Table 3. YY' axis shows the number of trends included in the analysis, while XX' the starting year. The hatched pixels represent regions with the significant trends ($|\omega/\sigma_{\omega}| > 2.0$).**

### 3.3.1 Global land and ocean

Small global DOD trends are recorded during the study period both over land and ocean (Table 3). However, distinguishable DOD trends are detected at specific regions. Prior studies have focused on satellite-based measurements detecting statistically significant AOD trends at global scale. Over oceanic areas, AOD trends based on MODIS Collection 6.0 are reported to be equal to 0.0050 decade$^{-1}$ and 0.0020 decade$^{-1}$ during 2000−2009 and 2000−2015, respectively (Alfaro-Contreras et al., 2017). SeaWiFS AOD retrievals recorded higher annual positive significant trends over ocean (0.00080 yr$^{-1}$) for a 13-year period (1998−2010) (Hsu et al., 2012). Recently, significant positive tendencies are documented for GLB (0.00066 yr$^{-1}$) using L3 Collection 6.1 MODIS/Terra measurements spanning from 2001 and 2016 (Che et al., 2019). In this study, significant AOD trends of 0.00052 yr$^{-1}$ and 0.00051 yr$^{-1}$ are revealed over GLB-O and GLB respectively (Fig. 8b), using geometric means at fine spatial resolution. The differences in trends magnitude among the studies are attributed to the different datasets, aggregation methods and temporal availability.

### 3.3.2 North Africa

Across North Africa, four sectors have been defined based on the sign of the DOD trends (see Figure 7) The first one consists of Central Sahara (CSA) where increasing DOD trends are mainly recorded (up to 0.023 yr$^{-1}$) (Fig. 10c). Voss and

Evan (2020) also reported similar DOD trends, in terms of sign and magnitude, based on MODIS/Aqua dataset over the period 2003−2018. At regional scale, positive significant DOD trends of 0.0021 $yr^{-1}$ determining those of AOD as expected (regional DOD to AOD trend ratio=0.84) due to the predominance of mineral particles in the area among other aerosol species (Fig. 10d). During different time frames, the sign of DOD trends remains mainly positive (Fig. 9), with intense (from 0.0044 to 0.0095 $yr^{-1}$) and significant results within the 2011− onward periods. Nevertheless, the time window is very short to infer the amplitude of the calculated trends.

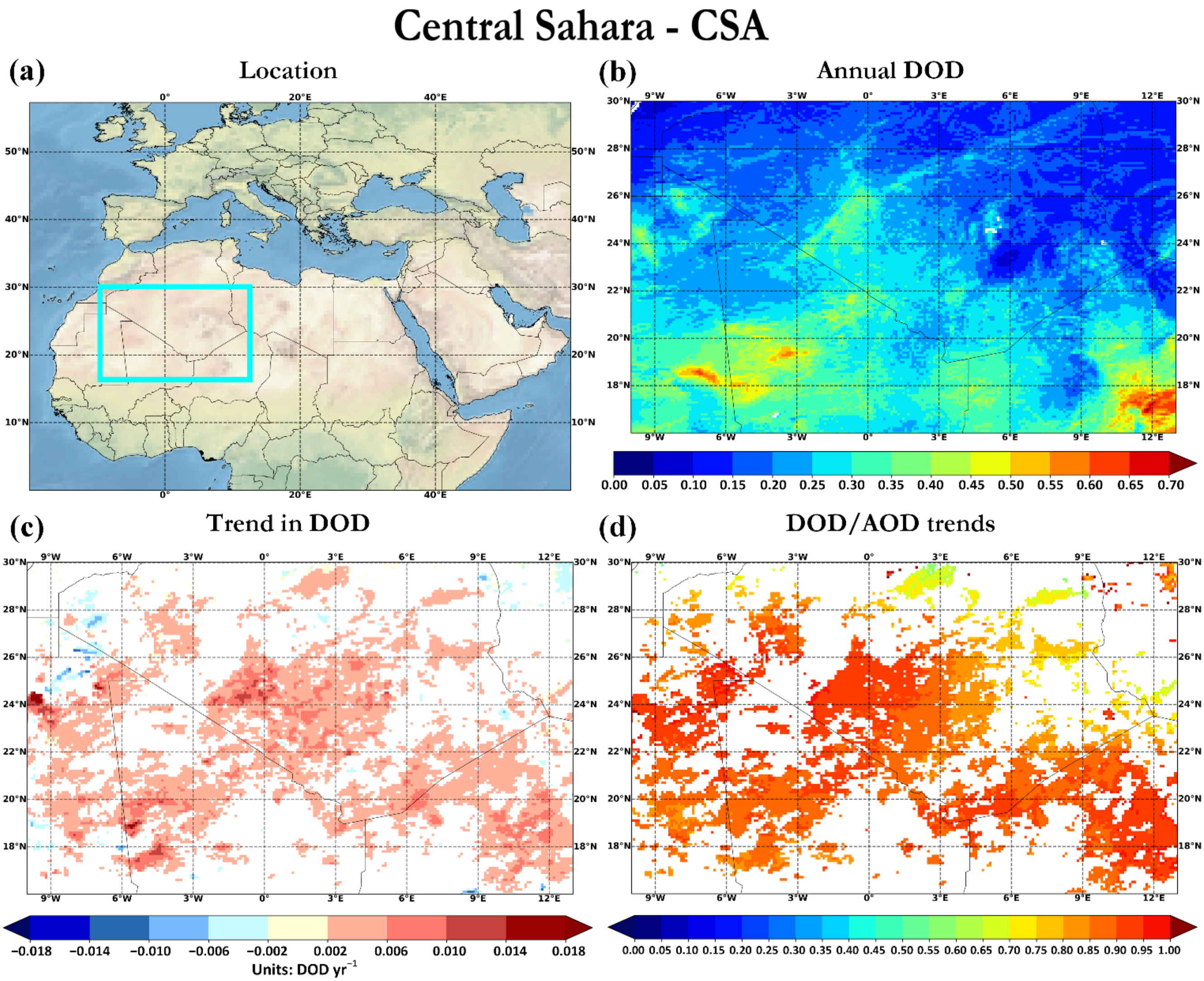

**Figure 10: (a) geographical boundaries, (b) annual DOD, (c) DOD geometric trends and (d) DOD to AOD trends ratio, for the Central Sahara.**

In the westernmost section of the Sahara Desert (WSA), in the majority of grid-cells (~73%) decreasing DOD tendencies are recorded (down to −0.015 $yr^{-1}$) whereas positive trends (up to 0.009 $yr^{-1}$) are evident at scattered pixels (~27%) within the domain (Fig. 11c). Overall, the total load (Fig. 8a) as well as the dust burden (Fig. 8b) have been decreased during the study period, but the magnitude of this reduction is relatively low and not statistically significant. This behavior is consistent regardless the spatial resolution or the approach for the calculation of regional values (i.e. arithmetic or geometric mean) (Figs. 8a and 8b). The same DOD trend pattern is also reflected using different time periods (Fig. 9).

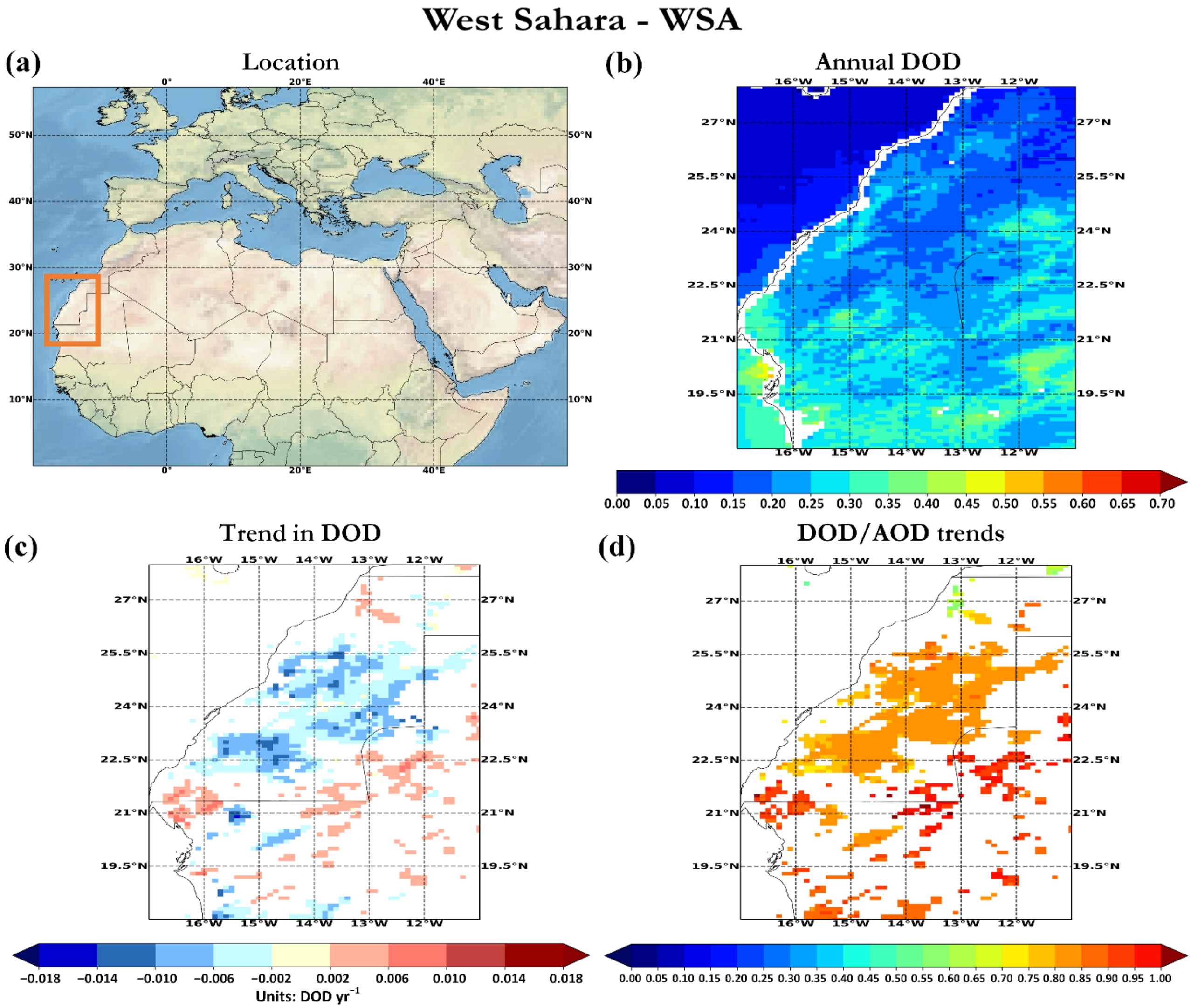

**Figure 11: Same as Fig. 10, but for the Western Sahara.**

In the eastern sector of the Sahara Desert (ESA), statistically significant negative DOD trends (down to −0.023 yr$^{-1}$) (Fig. 12c) are revealed as well as both for regional DOD (Fig. 8a) and AOD (Fig. 8b) trend thus indicating the predominant contribution of mineral particles to the total aerosol load. Reduction of the dust burden has also been recorded from MODIS/Terra dataset according to Voss and Evan (2020). Dust particles affect potentially total AOD across ESA indicating a regional DOD to AOD trend ratio of 1.06. Over the dust-affected areas of the planet, the DOD to AOD trends ratio range from negative (different trend sign) to higher than unity values. Since the dust burden modulate the total AOD over 'dusty' regions, the ratio between DOD and AOD is expected around unity. Higher ratios than unity are expected as the non-dust AOD signal decreases or increases and the DOD signal shows a reciprocal pattern. According to Fig. 9, two significant outcomes can be extracted in ESA. The magnitude, in absolute terms, of the decreasing DOD trends increases (down to $-0.0054$ yr$^{-1}$; 2012−2017) and the statistical significance is achieved for shorter time periods for increasing starting years.

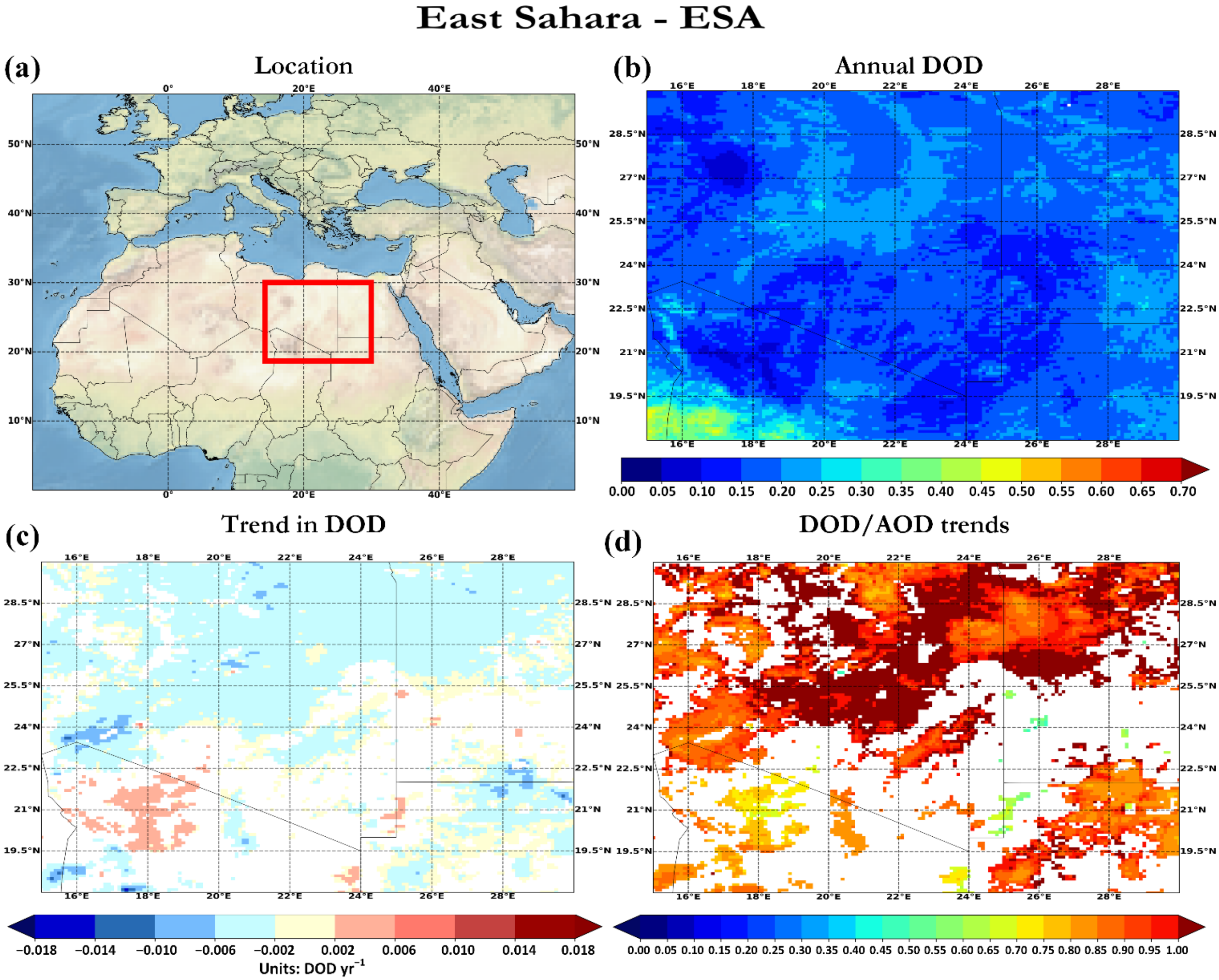

**Figure 12: Same as Fig. 10, but for the Eastern Sahara.**

Within the study period, the regional dust load decreases ($-0.0055$ yr$^{-1}$) in the Bodélé Depression (BOD) consisting the most active aeolian dust source of the planet (Prospero et al., 2002; Washington et al., 2006; Todd et al., 2007; Gkikas et al., 2021b). DOD trends range from $-0.021$ yr$^{-1}$ to $-0.003$ yr$^{-1}$ (Fig. 13c), corroborating the findings of the Voss and Evan (2020). For starting years between 2003−2010 the dust aerosol burden decreases (Fig. 9), with the most negative trend found during

2007−2014 (−0.015 yr$^{-1}$). As the starting year increases and the time length decreases, the magnitude of DOD trends become weaker. More specifically, the sign of DOD trends is shifted using 2011−2013 as starting years, but the results are not statistically significant. The latter indicates that DOD over the most active dust source of the planet becomes more intense during the last years. In order to better understand the reasons for the decreasing DOD trends across BOD, we investigated the correlation between the monthly MIDAS DODs and two meteorological variables, such as the wind speed (WS) at 10 m and the accumulated precipitation (STP) along with the volumetric soil water (Layer: 0-7 cm) (VSM), retrieved from ERA5 reanalysis products (Hersbach et al., 2018, 2020). Figure S11 displays the trend analysis of the aforementioned parameters over the area of BOD. The solid black box depicted in Fig. S11a refers to the area that is presented in Fig. 13. Based on Fig. S11a, except of the small area where strong negative trends are documented, there are also many scattered pixels of negative trends in the surrounding area (16–19°N - 15–20°E). According to Figs. 11b-d, it is evident that DOD values are related to temporal variability of applied parameters. Through time, dust amounts are strongly related to meteorology as well as geophysical factors. For instance, the increase of STP and VSM levels increases the wet dust deposition and decreases the dust erosion, causing the reduction of dust load. On the other hand, the increase of WS acting in favor of dust erosion thus increasing the dust amount. Across this region, increasing STP and VSM trends are documented, showing that the reduction of DOD levels is strongly related to the increase of STP and VSM. It should be mentioned that across this area the levels of WS and VSM provide a seasonal pattern, recording relatively low levels through the seasons of the year. During summer, the Intertropical Convergence Zone (ITCZ) location moves to higher latitudes and rapidly affects the amounts of WS and VSM across BOD. The revealed summertime STP and SVM trends are higher in terms of magnitude. In addition, positive trends have also been documented for WS. Generally, the increase of WS acting in favor of dust erosion thus increasing the dust amount. However, the level of increased WS are revealed relatively small and may not lead to changes of dust amount across BOD. To our knowledge, there is not observed changes of the surface reflectance that could influence the true level of MODIS AOD and providing suspicious tendencies, like those of Klingmüller et al. (2016) study in the area of Aral Sea, where the substantial trends in terms of magnitude are revealed and proved to be related to the land cover changes caused by the drying of the Aral Sea.

The aerosols' burden over the Sahara Desert is modulated by meteorological parameters affecting the dust emissions such as precipitation (Pozzer et al., 2015) and wind speed (Che et al., 2019). Based on model simulations, Pozzer et al. (2015) confirmed that positive AOD trends across Sahara Desert are linked to negative precipitation trends during 2001-2010. Decreasing precipitation levels reduces dust deposition and favors dust transport, leading to an increase in dust amounts. In addition, Che et al. (2019) reported that wind speed is the most critical feature for explaining the variance of AOD (by 29.8%). During the high dust seasons, the interannual variation of dust emissions is affected by wind speed and the NLLJ (in the southern Sahara dust sources) as well as by the Harmattan surge and Mediterranean depressions (in the northern Sahara dust sources) (Shi et al., 2021).

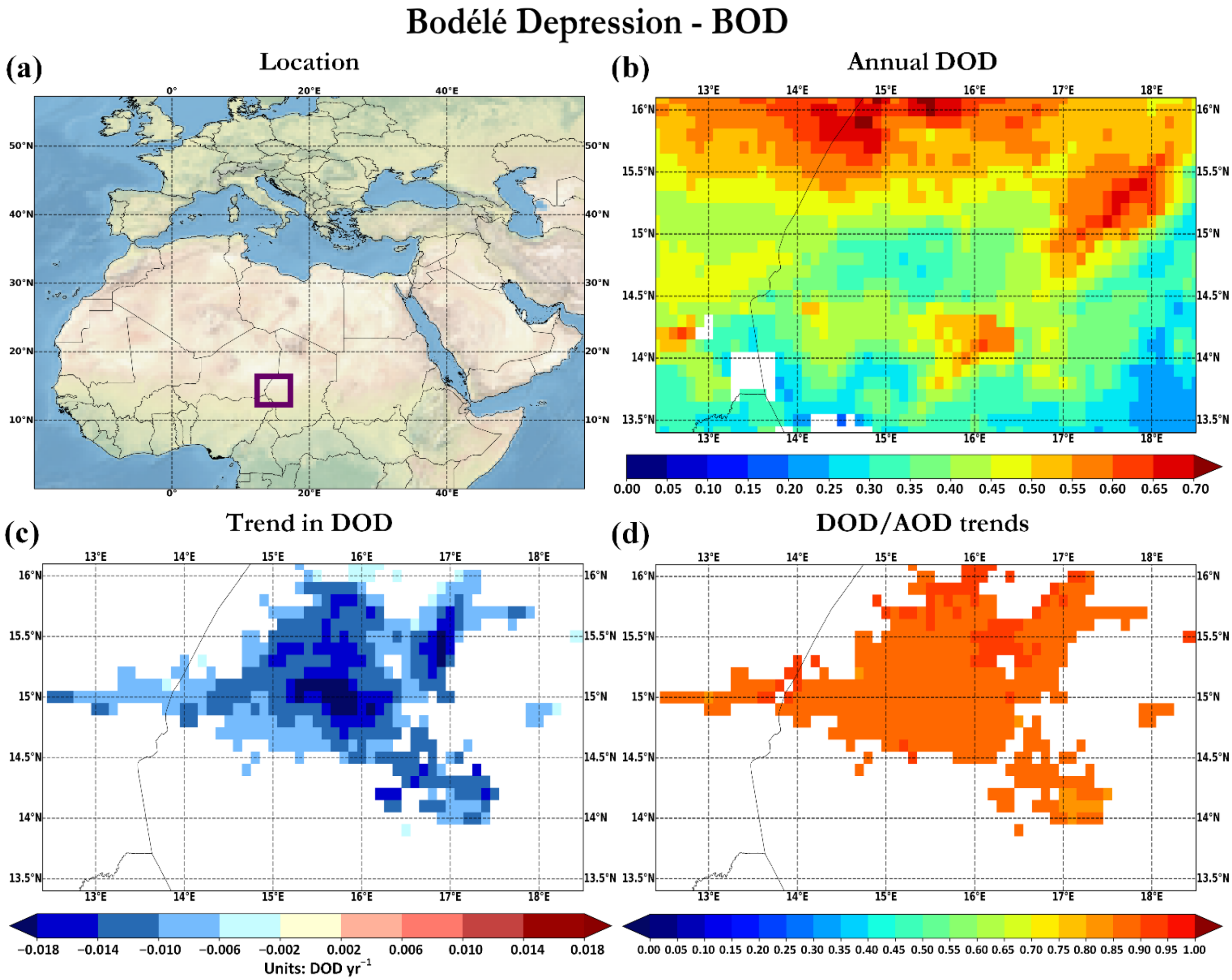

**Figure 13: Same as Fig. 10, but for the Bodélé Depression.**

### 3.3.3 Arabian Peninsula

The DOD tendencies over the Arabian Peninsula are presented separately for the northern (NAP) and the southern (SAP; including Jordan, Iraq and Syria) sectors. In both regions, positive trends (non-significant, Fig. 8a) are computed which are stronger in the southern parts of the Arabian Peninsula.

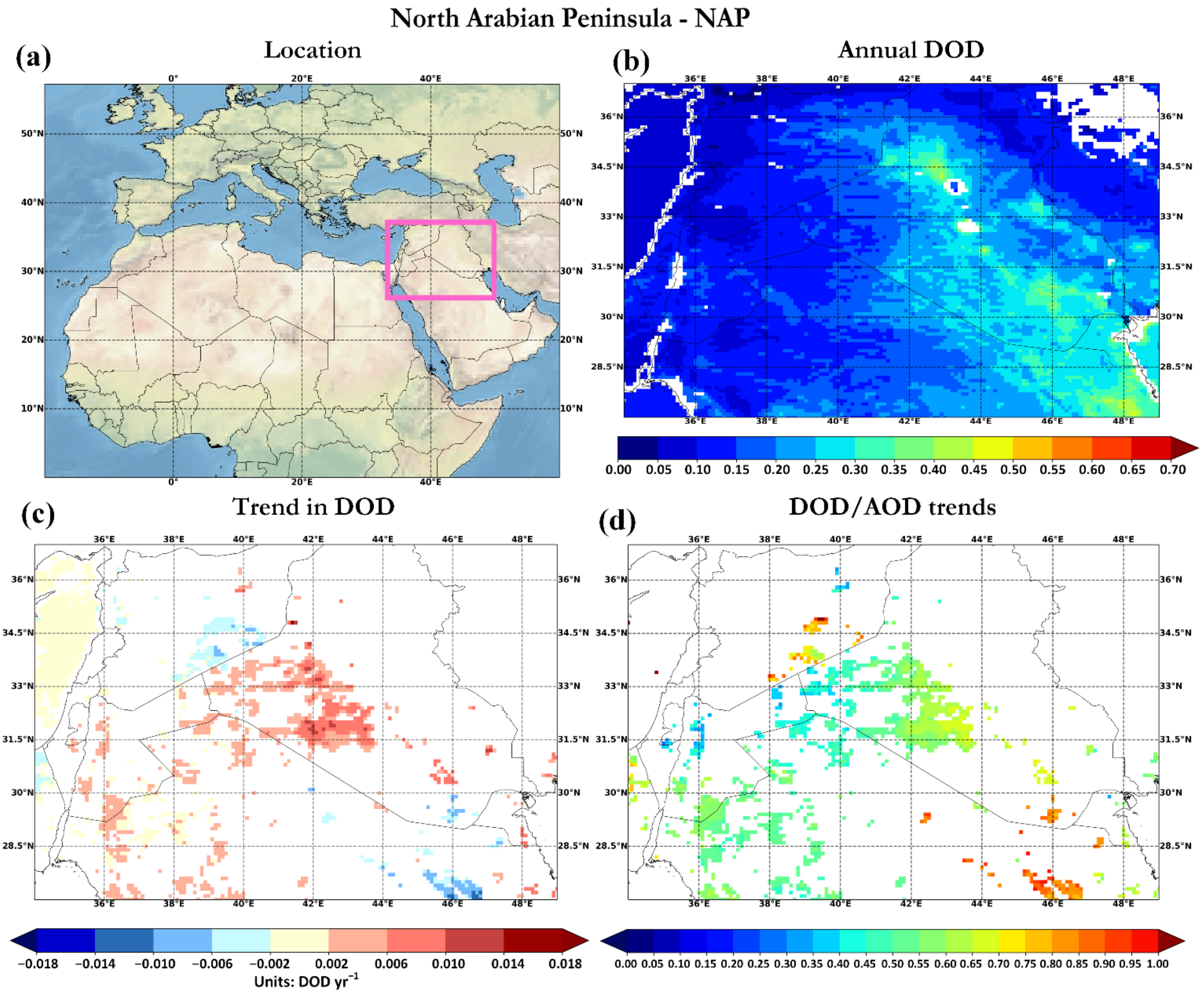

**Figure 14: Same as Fig. 10, but for the North Arabian Peninsula.**

Across Arabian Peninsula, the sign of the trend provides a bimodal pattern, revealing strong positive trends for time frames up to 2013 and followed by negative trends onwards (Fig. 9). Our findings are consistent with the revealed regime shift regarding dust activity in the Arabian Peninsula, as discussed in Notaro et al. (2015). The increased dust activity is also reflected in MIDAS DODs between 2008 and 2012, recording increased and stable annual DOD values (~0.2) compared to the previous 2003−2007 period DOD values (~0.15). Due to these sudden changes of dust amounts tendencies (from positive to negative), the regional DOD trends revealed non-significant within the entire study period (Fig. 8a). Klingmüller et al. (2016) documented increasing AOD trends during 2001−2012 followed by declining tendencies onwards, in agreement with our findings (Fig. 9). The predominant role of mineral particles on the total aerosol load across the Arabian Peninsula, is also reflected by the moderate-to-high DOD/AOD trend ratios (up to 0.65; Figs. 14d and 15d). Both increases in DOD and non-dust AOD explain the moderate in magnitude trend ratios.

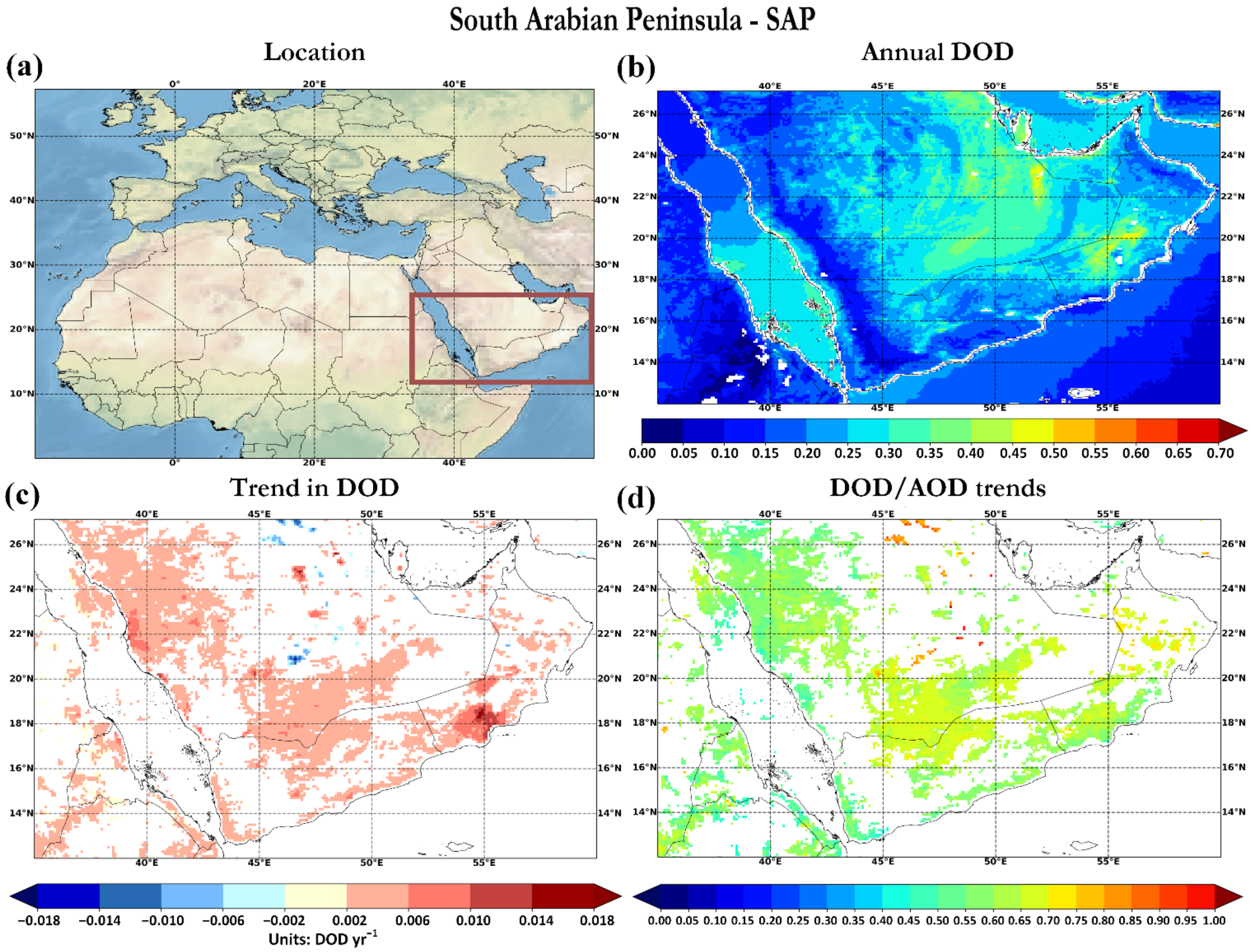

**Figure 15: Same as Fig. 10, but for the South Arabian Peninsula.**

In the last few decades, compelling inter-annual dust activity is documented in the Arabian Peninsula (Notaro et al., 2015). Numerous studies examined the temporal variability of aerosol loads in the Middle East, showing strong ascending tendencies (de Meij et al., 2012; Hsu et al., 2012; Yoon et al., 2014; Pozzer et al., 2015; Klingmüller et al., 2016; Che et al., 2019; Wei et al., 2019a). Klingmüller et al. (2016) revealed that the positive AOD trends in Middle East are associated with decreasing trends of Ångström exponent (AE) and fine mode fraction (FMF) indicating a shift towards a regime with stronger presence of coarse particles. These findings are in agreement with the increasing DOD trends documented in this study during the same study period (Fig. 9). Moreover, Klingmüller et al. (2016) implemented a multivariate linear model for annual AOD in order to identify the linkage of AOD trends with critical parameters such as the precipitation, the surface soil moisture and the surface wind speed. Soil moisture is the major controlling parameter in Saudi Arabia and Iraq whereas precipitation dominates in Iran. For all regions, the addition of surface wind speed as independent parameter upgraded the model performance. Moreover, Che et al. (2019) also used a multiple linear regression model to investigate the relationship of AOD with specific meteorological parameters. The most appropriate ones, in terms of statistical significance, are chosen to enhance the model performance. Across Middle East, the major controlling meteorological parameter for AOD variance is the sea level pressure (60.9% of total AOD explained variation) and the wind speed, highlighting the large impact of synoptic systems on dust burden over the area.

### 3.3.4 Mediterranean

The Mediterranean (MED) basin is a region of great concern due to high inter-annual variability of aerosol loadings and types (Floutsi et al., 2016). In this study, MED presents significant DOD trends ranging from −0.009 yr$^{-1}$ to 0.006 yr$^{-1}$ (Fig. 16c). The regional analysis documents strong declining significant DOD (Fig. 8a) and AOD (Fig. 8b) tendencies across the MED basin. Negative DOD trends are also revealed during different sub-periods (Fig. 9). The DOD to AOD trends ratio shows a latitudinal reduction moving from northern African coasts to the northern parts of the Mediterranean (Fig. 16d). Higher ratio values are documented in South Mediterranean-North African coast region (0.3-1.94, median = 0.71) (Lat: 30.0−38.0 °N; Lon: 6.0 °W−30.0 °E) compared to North Mediterranean (0.21-0.91, median = 0.45) (Lat: 38.0−45.0 °N; Lon: 1.0 °W−27.0 °E). Dust particles originated from North African and Middle East deserts driven by low pressure systems (cyclones) can be transported towards MED (Gkikas et al., 2015), providing relatively high AOD values at the southern parts. Mineral particles are recorded mainly in summer, spring and winter in Western, Central and East MED, respectively (Floutsi et al., 2016; Gkikas et al., 2013; 2016; 2021b). Across the north sector of MED, lower AOD values are associated with higher FMF values due to the prevailing anthropogenic fine aerosols (Floutsi et al., 2016). The latter could also be observed from the negligible DOD trends there (Fig. 16c).

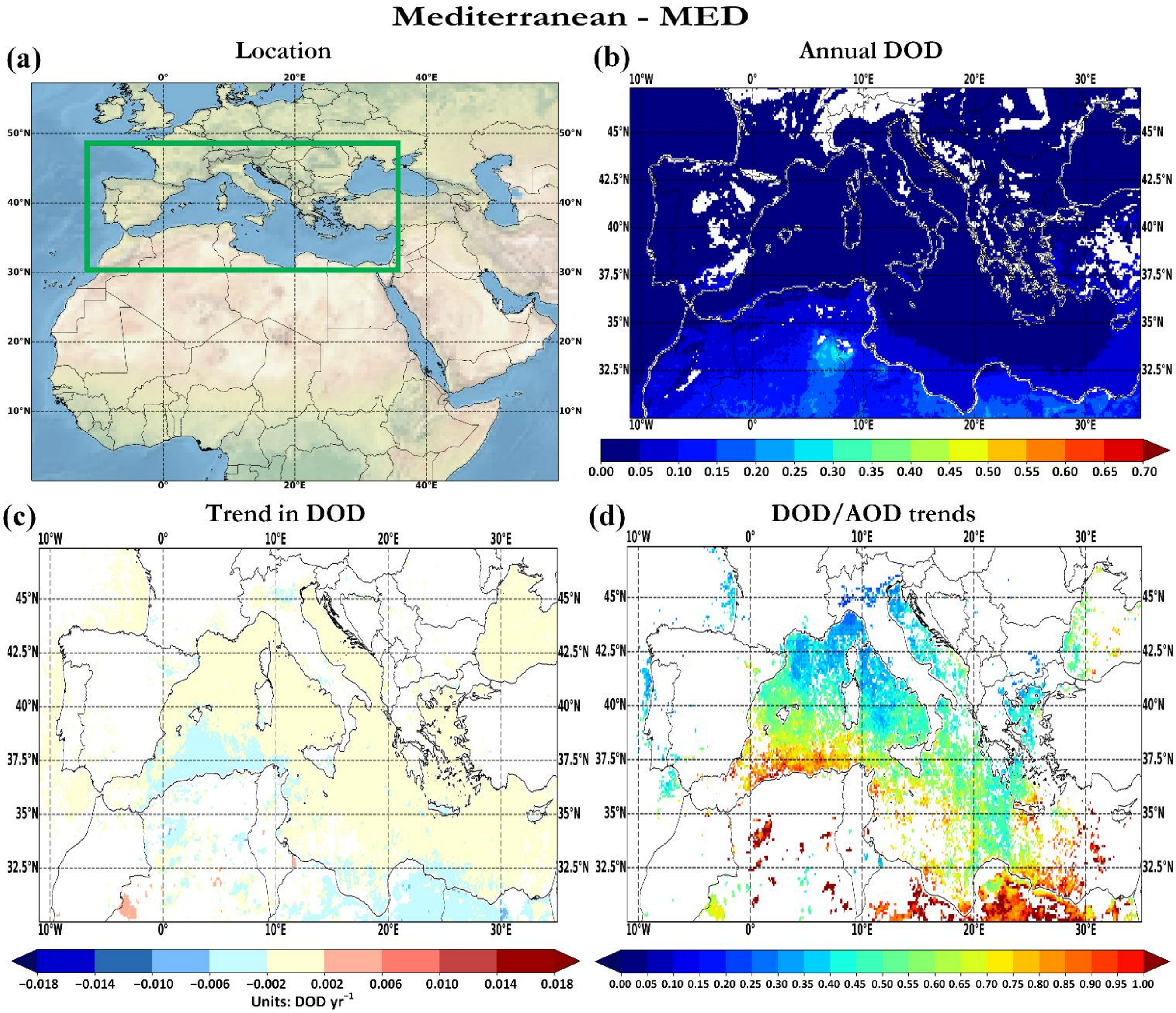

**Figure 16: Same as Fig. 10, but for the Mediterranean Basin.**

Earlier studies investigated the temporal AOD variability in the broader Mediterranean basin, reporting declining tendencies for the last two decades (Papadimas et al., 2008; de Meij et al., 2012; Hsu et al., 2012; Yoon et al., 2014; Pozzer et al., 2015; Floutsi et al., 2016; Che et al., 2019). Across this region, Floutsi et al. (2016) reported significant decreasing AOD trends of −0.0030 yr$^{-1}$ over the period 2002−2014. Additionally, Nabat et al, 2013, reported decreasing DOD trends (−0.0045 yr$^{-1}$) across northern Africa. Both studies corroborate with the findings of this study where the overwhelming majority DOD trends are primarily slightly negative (Fig. 16c).

### 3.3.5 Thar and Gobi Deserts

Across the western part of Indo-Gangetic Plain, in the northwest area of the Indian Subcontinent, the Thar Desert (THA) is situated. THA region depicts significant decreasing DOD trends (down to $-0.017$ yr$^{-1}$) (Fig. 17c) modulating the corresponding declining AOD tendencies as indicated by the relatively high DOD/AOD trends ratio (0.67; Fig. 17d). The statistical significance of DOD trends, which are always negative regardless the sub-period, is strongly affected by the starting year as well as the length of the time interval in which the tendencies are computed (Fig. 9). More specifically, negative and not statistically significant DOD trends are observed for all time periods beginning from 2005. During the last two decades, strong negative temporal trends are recorded for OMI ultraviolet aerosol index (Hammer et al., 2018) along with AOD (Che et al., 2019) and DOD (Voss and Evan, 2020) across THA. The reduction of dust abundance over THA is mainly attributed to the increase of the rainfall and soil moisture enhancing wet dust deposition and reducing dust erosion during pre-monsoon (Pandey et al., 2017; Jin and Wang, 2018).

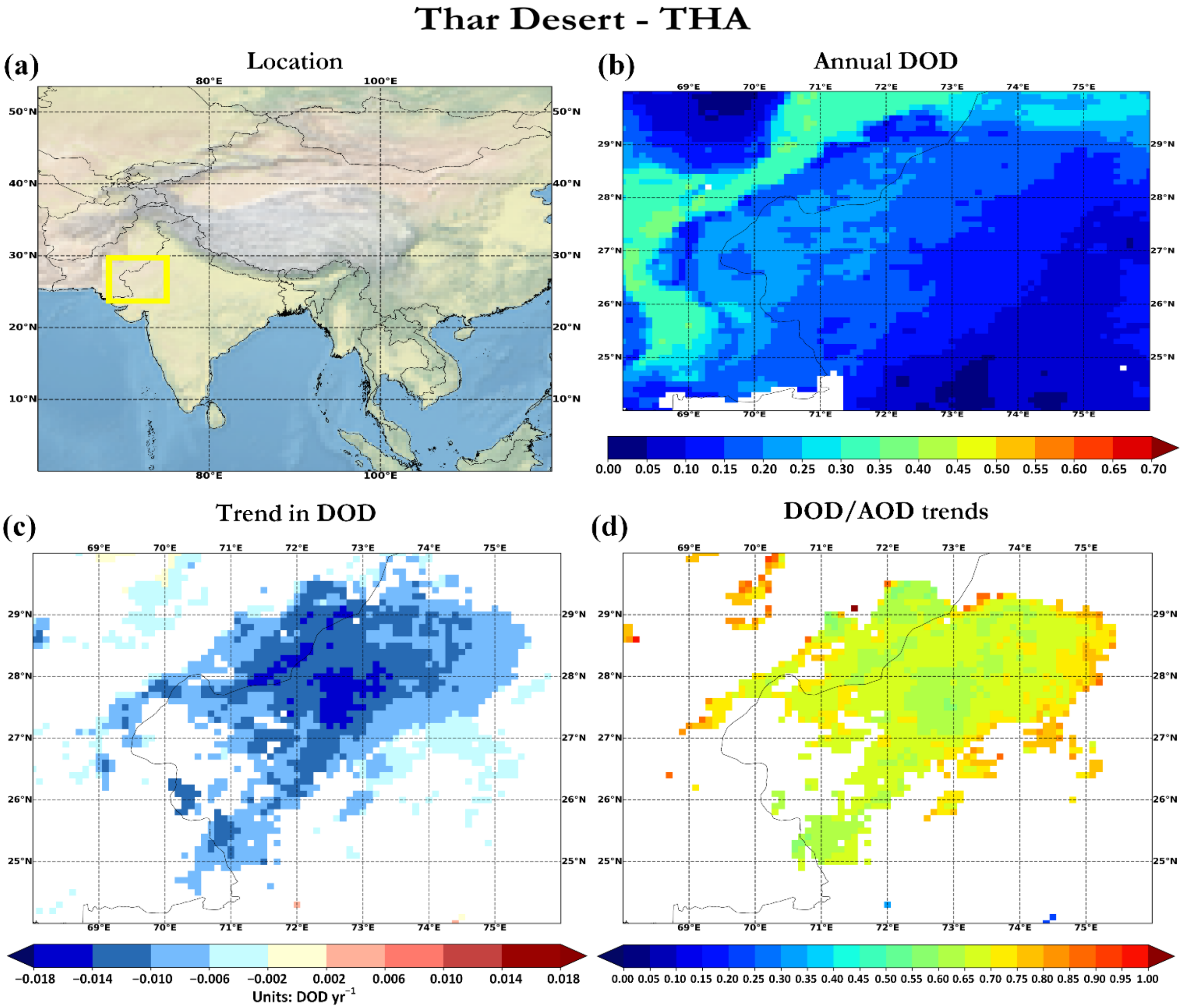

**Figure 17: Same as Fig. 10, but for the Thar Desert.**

The Gobi Desert (GOB) resides between the north part of China and the southern sector of Mongolia (East Asia). In this region, statistically significant DOD trends, ranging from −0.011 $yr^{-1}$ to 0.004 $yr^{-1}$, are reported (Fig. 18c), in agreement (both in sign and magnitude) with those reported by Che et al. (2019) and Voss and Evan (2020) for AOD and DOD, respectively. At a regional level, slightly negative DOD (−0.00071 $yr^{-1}$) and AOD (−0.0010 $yr^{-1}$) trends, and statistically significant at 90% confidence level ($|\omega/\sigma_{\omega}|>1.65$), are computed (Fig. 8). Nevertheless, for time periods onwards 2005, the DOD trends are statistically significant at 95% confidence level (Fig. 9). These temporal DOD trends corroborate with Filonchyk et al. (2019), who computed AOD trends equal to −0.004 $decade^{-1}$ and −0.002 $decade^{-1}$ for MODIS/Terra and MISR measurements, respectively, over the period 2000−2017. In addition, GOB AOD trends are strongly influenced by the presence of dust particles, recording moderate median DOD to AOD trends ratio value of 0.62 (Fig. 18d).

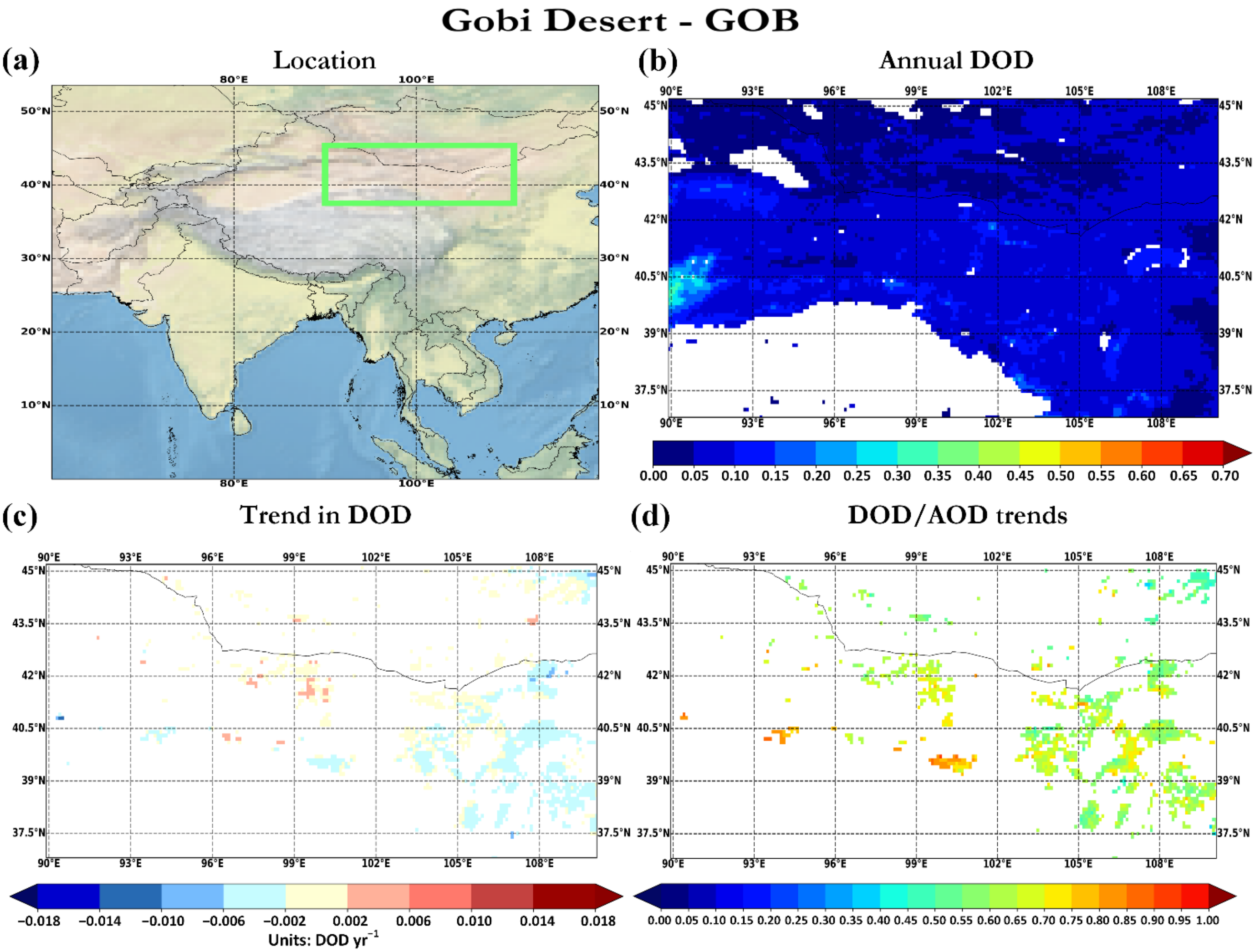

**Figure 18: Same as Fig. 10, but for the Gobi Desert.**

An et al. (2018) conducted a comprehensive analysis to investigate the potential factors driving the reduction of sand and dust storms, taking place mainly in springtime, in East Asia between 2006 and 2017. In the aforementioned study, across GOB, the mean surface dust concentration was declined by −31.71 μg m$^{-3}$ yr$^{-1}$ (−12.24 %). These declining trends are regulated by changes in the surface conditions (e.g. vegetation coverage) which are strongly linked to precipitation, soil moisture, ambient temperature and human activities. The increasing trends in vegetation coverage are observed using the Normalized Difference Vegetation Index (NDVI) (0.0006 yr$^{-1}$) from MODIS and are linked with the ascending tendencies of the precipitation (0.002 mm day$^{-1}$ yr$^{-1}$) and volumetric soil moisture at 0-0.1 m depth (0.316 yr$^{-1}$). All these factors converge towards the reduction of emitted amounts of dust aerosols. Over East Asia, the frequency and intensity of dust outbreaks have been decreased during the springtime (An et al., 2018). Dust particles are primarily uplifted into the surrounding air across this region due to massive winds accompanied by cold air from northern latitudes. The decreasing frequency and intensity of dust outbreaks can be explained by the declining tendencies of the north wind components, documented during 2007−2016. The latter is associated with the decline of 1) Polar Vortex intensity, 2) north-to-south mean surface level pressure gradient and 3) meridional wind component magnitude.

## 4 Summary and conclusions

Airborne dust affects the global and regional climate via the induced perturbation of the solar and terrestrial radiation fields. Therefore, the investigation of DOD temporal variations is crucial to assess its climatic role as well as the multifarious impacts within the Earth-Atmosphere system and humans' health. The present study deals with the investigation of the annual and seasonal trends of AOD and DOD, both at global and regional scales over the period 2003–2017, relying on the MIDAS fine resolution dataset. Taking advantage of the MIDAS strong capabilities, the DOD trends have been analyzed: (i) by considering different aggregation approaches (i.e. arithmetic and geometric means), (ii) at fine and coarse spatial resolutions, (iii) applying and not applying temporal filters (iv) at annual, seasonal and sub-period time scales (i.e. sliding window) and (v) their contribution to the corresponding tendencies of the total aerosol optical depth. Based on this holistic approach, it is provided a complete overview about the temporal variability of dust loads addressing jointly all the factors determining the sign, the magnitude and the statistical significance of the calculated trends.

The validity of the MIDAS DOD trends has been investigated with respect to AERONET cAOD data. This analysis encompassed that MIDAS tendencies are capable to follow those of AERONET either for increasing (at 26 out of 30 stations, 86.7%) or decreasing (at 7 out of 11 stations, 63.6%) trends. Point-to-point investigation of the DOD-cAOD trends highlighted the accurate, in terms of magnitude and statistical significance, MIDAS DOD trends either across "dusty" sites or downwind areas.

The sensitivity analysis between coarse and fine spatial resolution revealed that the magnitude of AOD and DOD trends are lower for the coarse spatial resolution data. On a regional basis, the calculated AOD/DOD trends revealed a very good agreement in terms of trend magnitude for both spatial scales. In general, coarse resolution data provide better spatial coverage, however, detailed information, in spatial terms, is when fine resolution data are utilized. In addition, the sensitivity analysis on the different aggregation approaches revealed that the arithmetic-based trends are larger than those of the geometric-based ones (from 52.87 to 91.77%) all over the globe. The only exception was found only for AOD at coarse spatial resolution. Lastly, the sensitivity analysis on the temporal filtering in trend calculations indicated new regions (e.g. across oceanic territories) with unphysical unfiltered AOD trends. In addition, unfiltered trends led to poorer performance of MIDAS DOD trends against AERONET retrievals.

Based on our analysis, increasing DOD trends are obtained across the Central Sahara and the Arabian Peninsula whereas opposite tendencies are recorded over the Eastern and Western Sahara, the Thar and Gobi Deserts, in the Bodélé Depression and in southern Mediterranean. On the seasonal basis, the maximum positive DOD trends are displayed in the Central Sahara and Middle East area during summertime. During spring, the strongest reductions of the dust burden have been revealed at the Bodélé Depression whereas reverse tendencies have been recorded in the Western and Eastern Sahara and in the Thar and Taklamakan Deserts during summer. Similarly, the most negative trends were observed at spring over the Gobi Desert. Positive trends across the area extending from North Atlantic Ocean to the eastern Caribbean Sea are observed in spring.

At global scale and separately over continents and oceans, negligible and non-significant DOD trends are found. A similar analysis for 9 specific regions of the planet has been performed revealing evident trends which are not however all of them statistically significant. More specifically, strong DOD trends were documented in Central (0.0021 $yr^{-1}$) and East (−0.0018 $yr^{-1}$) Sahara, Bodélé Depression (−0.0055 $yr^{-1}$), Mediterranean (−0.0011 $yr^{-1}$) and Thar Desert (−0.0053 $yr^{-1}$). In contrast, non-significant regional DOD trends were depicted in the Arabian Peninsula and the Gobi Desert. At a regional scale, the calculated trends vary in terms of sign, magnitude and statistical significance, depending on the sub-period, thus indicating a strong interannual variation of dust aerosols' load within the period 2003–2017. In the majority of the regions of interest, including also downwind areas, the variations of the total aerosol load are driven by those of mineral particles.

The obtained findings from the current study highlight the applicability of the MIDAS dataset for detecting dust temporal across various spatial scales. The high spatiotemporal resolution of MIDAS provides the opportunity to complement and further expand the existing knowledge on this critical aspect, yet not well covered in the field of dust research. Likewise, by comparing AOD and DOD tendencies, it is feasible the assessment of mineral particles' role on the variations of the total aerosol load. Our results could be incorporated in chemical models, either for assessing the various impacts of dust and non-dust particles or for evaluating trends based on numerical simulations, and to further improve their calibration and forecast performance. Moreover, the obtained findings here can be used for the interpretation of the trends of the radiation fluxes at the surface and at the top of the atmosphere obtained by observations or atmospheric-aerosol models (Chaibou et al., 2020). The recently published Sixth Assessment Report (AR6) of the Intergovernmental Panel on Climate Change (IPCC) states that the increase of the global dust load causes a reduction of the effective radiative forcing (ERF) by −0.25 $Wm^{-2}$ (Andrews et al., 2017; Forster et al., 2021). Therefore, fluctuations of the dust atmospheric load provide a valuable information in order to understand the associated impacts on past, current and future climate. Finally, the current study focused mainly on the description of dust optical depth trends providing also a preliminary interpretation of the obtained findings. Nevertheless, an in-depth analysis (a follow up study) is ongoing by investigating the role of critical meteorological variables (e.g. wind) as well as of other determinant geophysical factors (e.g. soil moisture, vegetation, land coverage) on the configuration of DOD trends.

## Acknowledgments

We acknowledge support of this work by the project “PANhellenic infrastructure for Atmospheric Composition and climatE change” (MIS 5021516) which is implemented under the Action “*Reinforcement of the Research and Innovation Infrastructure*”, funded by the Operational Programme "Competitiveness, Entrepreneurship and Innovation" (NSRF 2014-2020) and co-financed by Greece and the European Union (European Regional Development Fund). The MIDAS dataset has been developed in the framework of the DUST-GLASS project (grant no. 749461; European Union’s Horizon 2020 Research and Innovation programme under the Marie Skłodowska-Curie Actions. Antonis Gkikas acknowledges support by the Hellenic Foundation for Research and Innovation (H.F.R.I.) under the “2nd Call for H.F.R.I. Research Projects to support Post-Doctoral Researchers” (Project Acronym: ATLANTAS, Project number: 544). Vassilis Amiridis acknowledges support from the European Research Council (grant no. 725698; D-TECT). Stelios Kazadzis acknowledges the International Network to Encourage the Use of Monitoring and Forecasting Dust Products (inDust) COST Action CA16202. We gratefully acknowledge the data provided by AERONET network and we wish to express our appreciation to the operators of stations for their efforts on running the instruments.

## Author contribution

SAL was responsible for the whole analysis and the preparation of the initial manuscript with support from VS. AG processed the MIDAS dataset and had an advisory role in the relevant parts of the study. AK and SK conceptualized the main objective of the manuscript and supervised the progress. VA provided feedback on the scientific discussions. All authors contributed to the revision and the final editing of the initial manuscript.

## Competing interests

The authors declare that they have no competing interests.

## References

Adesina, A. J., Kumar, K. R., Sivakumar, V. and Piketh, S. J.: Intercomparison and assessment of long-term (2004–2013) multiple satellite aerosol products over two contrasting sites in South Africa, J. Atmos. Solar-Terrestrial Phys., 148, 82–95, https://doi.org/10.1016/j.jastp.2016.09.001, 2016.

Alfaro-Contreras, R., Zhang, J., Reid, J. S. and Christopher, S.: A study of 15-year aerosol optical thickness and direct shortwave aerosol radiative effect trends using MODIS, MISR, CALIOP and CERES, Atmos. Chem. Phys., 17(22), 13849–13868, https://doi.org/10.5194/acp-17-13849-2017, 2017.

Alizadeh-Choobari, O., Zawar-Reza, P., Sturman, A.: The global distribution of mineral dust and its impacts on the climate system: A review, Atmos. Res., 138, 152–165, 1174, https://doi.org/10.1016/j.atmosres.2013.11.007, 2014a.

Alizadeh-Choobari, O., Zawar-Reza, P., Sturman, A.: The “wind of 120 days” and dust storm activity over the Sistan Basin, Atmos. Res., 143, 328–341, https://doi.org/10.1016/j.atmosres.2014.02.001, 2014b.

Alizadeh-Choobari, O., Sturman, A. and Zawar-Reza, P.: A global satellite view of the seasonal distribution of mineral dust and its correlation with atmospheric circulation, Dyn. Atmos. Ocean., 68, 20–34, https://doi.org/10.1016/j.dynatmoce.2014.07.002, 2014c.

Amiridis, V., Wandinger, U., Marinou, E., Giannakaki, E., Tsekeri, A., Basart, S., Kazadzis, S., Gkikas, A., Taylor, M., Baldasano, J., and Ansmann, A.: Optimizing CALIPSO Saharan dust retrievals, Atmos. Chem. Phys., 13, 12089–12106, https://doi.org/10.5194/acp-13-12089-2013, 2013.

Amiridis, V., Marinou, E., Tsekeri, A., Wandinger, U., Schwarz, A., Giannakaki, E., Mamouri, R., Kokkalis, P., Binietoglou, I., Solomos, S., Herekakis, T., Kazadzis, S., Gerasopoulos, E., Proestakis, E., Kottas, M., Balis, D., Papayannis, A., Kontoes, C., Kourtidis, K., Papagiannopoulos, N., Mona, L., Pappalardo, G., Le Rille, O., and Ansmann, A.: LIVAS: a 3-D multi-wavelength aerosol/cloud database based on CALIPSO and EARLINET, Atmos. Chem. Phys., 15, 7127–7153, https://doi.org/10.5194/acp15-7127-2015, 2015.

An, L., Che, H., Xue, M., Zhang, T., Wang, H., Wang, Y., Zhou, C., Zhao, H., Gui, K., Zheng, Y., Sun, T., Liang, Y., Sun, E., Zhang, H. and Zhang, X.: Temporal and spatial variations in sand and dust storm events in East Asia from 2007 to 2016: Relationships with surface conditions and climate change, Sci. Total Environ., 633, 452–462, https://doi.org/10.1016/j.scitotenv.2018.03.068, 2018.

Andrews, T., Betts, R. A., Booth, B. B. B., Jones, C. D., and Jones, G. S.: Effective radiative forcing from historical land use change, Clim. Dynam., 48, 3489–3505, https://doi.org/10.1007/s00382-016-3280-7, 2017.

Babu, S. S., Manoj, M. R., Moorthy, K. K., Gogoi, M. M., Nair, V. S., Kompalli, S. K., Satheesh, S. K., Niranjan, K., Ramagopal, K., Bhuyan, P. K. and Singh, D.: Trends in aerosol optical depth over Indian region: Potential causes and impact indicators, J. Geophys. Res. Atmos., 118(20), 11,794-11,806, https://doi.org/10.1002/2013JD020507, 2013.

Basart, S., Pérez, C., Cuevas, E., Baldasano, J. M., and Gobbi, G. P.: Aerosol characterization in Northern Africa, Northeastern Atlantic, Mediterranean Basin and Middle East from direct-sun AERONET observations, Atmos. Chem. Phys., 9, 8265–8282, https://doi.org/10.5194/acp-9-8265-2009, 2009.

Chaibou, A. A. S., Ma, X., and Sha, T.: Dust radiative forcing and its impact on surface energy budget over West Africa, Scientific Reports, 10, https://doi.org/10.1038/s41598-020-69223-4, 2020.

Che, H., Qi, B., Zhao, H., Xia, X., Eck, T. F., Goloub, P., Dubovik, O., Estelles, V., Cuevas-Agulló, E., Blarel, L., Wu, Y., Zhu, J., Du, R., Wang, Y., Wang, H., Gui, K., Yu, J., Zheng, Y., Sun, T., Chen, Q., Shi, G., and Zhang, X.: Aerosol optical properties and direct radiative forcing based on measurements from the China Aerosol Remote Sensing Network (CARSNET) in eastern China, Atmos. Chem. Phys., 18, 405–425, https://doi.org/10.5194/acp-18-405-2018, 2018.

Che, H., Gui, K., Xia, X., Wang, Y., Holben, B. N., Goloub, P., Cuevas-Agulló, E., Wang, H., Zheng, Y., Zhao, H., and Zhang, X.: Large contribution of meteorological factors to inter-decadal changes in regional aerosol optical depth, Atmos. Chem. Phys., 19, 10497–10523, https://doi.org/10.5194/acp-19-10497-2019, 2019.

Chen, J. L., Pekker, T., Wilson, C. R., Tapley, B. D., Kostianoy, A. G., Cretaux, J. F. and Safarov, E. S.: Long-term Caspian Sea level change, Geophys. Res. Lett., 44(13), 6993–7001, https://doi.org/10.1002/2017GL073958, 2017.

Clarisse, L., Clerbaux, C., Franco, B., Hadji-Lazaro, J., Whitburn, S., Kopp, A. K., Hurtmans, D., and Coheur, P.-F.: A Decadal Data Set of Global Atmospheric Dust Retrieved From IASI Satellite Measurements, J. Geophys. Res.-Atmos., 124, 1618–1647, https://doi.org/10.1029/2018JD029701, 2019.

Dahutia, P., Pathak, B., and Bhuyan, P. K.: Aerosols characteristics, trends and their climatic implications over Northeast India and adjoining South Asia, Int. J. Climatol., 38, 1234–1256, https://doi.org/10.1002/joc.5240, 2017.

de Meij, A., Pozzer, A. and Lelieveld, J.: Trend analysis in aerosol optical depths and pollutant emission estimates between 2000 and 2009, Atmos. Environ., 51, 75–85, https://doi.org/10.1016/j.atmosenv.2012.01.059, 2012.

Dubovik, O. and King, M. D.: A flexible inversion algorithm for retrieval of aerosol optical properties from Sun and sky radiance measurements, J. Geophys. Res., 105, 20673–20696, https://doi.org/10.1029/2000JD900282, 2000.

Elguindi, N., Solmon, F., Turuncoglu, U.: Quantifying some of the impacts of dust and other aerosol on the Caspian Sea region using a regional climate model. Clim. Dyn., 46, 41–55, https://doi.org/10.1007/s00382-015-2566-5, 2016.

Evan, A. T., Dunion, J., Foley, J. A., Heidinger, A. K., and Velden, C. S.: New evidence for a relationship between Atlantic tropical cyclone activity and African dust outbreaks, Geophysical Research Letters, 33, https://doi.org/10.1029/2006GL026408, 2006.

Evan, A. T., Flamant, C., Gaetani, M., and Guichard, F.: The past, present and future of African dust, Nature, 531, 493–495, https://doi.org/10.1038/nature17149, 2016.

Fréville, H., Chami, M. and Mallet, M.: Analysis of the Transport of Aerosols over the North Tropical Atlantic Ocean Using Time Series of POLDER/PARASOL Satellite Data, Remote Sens., 12, 757, https://doi.org/10.3390/rs12050757, 2020.

Forster, P., Storelvmo, T., Armour, K., Collins, W., Dufresne, J. L., Frame, D., Lunt, D. J., Mauritsen, T., Palmer, M. D., Watanabe, M., Wild, M., Zhang H.: The Earth's Energy Budget, Climate Feedbacks, and Climate Sensitivity. In: Climate Change 2021: The Physical Science Basis. Contribution of Working Group I to the Sixth Assessment Report of the Intergovernmental Panel on Climate Change [Masson-Delmotte, V., P. Zhai, A. Pirani, S. L. Connors, C. Péan, S. Berger, N. Caud, Y. Chen, L. Goldfarb, M. I. Gomis, M. Huang, K. Leitzell, E. Lonnoy, J. B. R. Matthews, T. K. Maycock, T. Waterfield, O. Yelekçi, R. Yu and B. Zhou (eds.)]. Cambridge University Press. In Press, 2021.

Filonchyk, M., Yan, H., Zhang, Z., Yang, S., Li, W. and Li, Y.: Combined use of satellite and surface observations to study aerosol optical depth in different regions of China, Sci. Rep., 9 (1), 1–15, doi:10.1038/s41598-019-42466-6, 2019.

Floutsi, A. A., Korras-Carraca, M. B., Matsoukas, C., Hatzianastassiou, N. and Biskos, G.: Climatology and trends of aerosol optical depth over the Mediterranean basin during the last 12 years (2002-2014) based on Collection 006 MODIS-Aqua data, Sci. Total Environ., 551–552, 292–303, https://doi.org/10.1016/j.scitotenv.2016.01.192, 2016.

Gelaro, R, McCarty, W., Suárez, M. J., Todling, R., Molod, A., Takacs, L., Randles, C. A., Darmenov, A., Bosilovich, M. G., Reichle, R., Wargan, K., Coy, L., Cullather, R., Draper, C., Akella, S., Buchard, V., Conaty, A., da Silva, A. M., Gu, W., Kim, G., Koster, R., Lucchesi, R., Merkova, D., Nielsen, J. E., Partyka, G., Pawson, S., Putman, W., Rienecker, M., Schubert, S. D., Sienkiewicz, M., and Zhao, B.: The Modern-Era Retrospective Analysis for Research and Applications, Version 2 (MERRA-2), J. Climate, 30, 5419–5454, https://doi.org/10.1175/JCLI-D-16-0758.1, 2017.

Giles, D. M., Holben, B. N., Eck, T. F., Sinyuk, A., Smirnov, A., Slutsker, I., Dickerson, R. R., and Thompson, A. M., and Schafer, J. S.: An analysis of AERONET aerosol absorption properties and classifications representative of aerosol source regions, J. Geophys. Res., 117, D17203, https://doi.org/10.1029/2012JD018127, 2012.

Giles, D. M., Sinyuk, A., Sorokin, M. G., Schafer, J. S., Smirnov, A., Slutsker, I., Eck, T. F., Holben, B. N., Lewis, J. R., Campbell, J. R., Welton, E. J., Korkin, S. V., and Lyapustin, A. I.: Advancements in the Aerosol Robotic Network (AERONET) Version 3 database – automated near-real-time quality control algorithm with improved cloud screening for Sun photometer aerosol optical depth (AOD) measurements, Atmos. Meas. Tech., 12, 169–209, https://doi.org/10.5194/amt-12-169-2019, 2019.

Ginoux, P., Prospero, J. M., Gill, T. E., Hsu, N. C., and Zhao, M.: Global-scale attribution of anthropogenic and natural dust sources and their emission rates based on MODIS Deep Blue aerosol products, Rev. Geophys., 50, RG3005, https://doi.org/10.1029/2012RG000388, 2012.

Gkikas, A., Hatzianastassiou, N., Mihalopoulos, N., Katsoulis, V., Kazadzis, S., Pey, J., Querol, X., and Torres, O.: The regime of intense desert dust episodes in the Mediterranean based on contemporary satellite observations and ground measurements, Atmos. Chem. Phys., 13, 12135–12154, https://doi.org/10.5194/acp-13-12135-2013, 2013.

Gkikas, A., Houssos, E. E., Lolis, C. J., Bartzokas, A., Mihalopoulos, N., and Hatzianastassiou, N.: Atmospheric circulation evolution related to desert-dust episodes over the Mediterranean, Q. J. Roy. Meteor. Soc., 141, 1634–1645, https://doi.org/10.1002/qj.2466, 2015.

Gkikas, A., Basart, S., Hatzianastassiou, N., Marinou, E., Amiridis, V., Kazadzis, S., Pey, J., Querol, X., Jorba, O., Gassó, S., and Baldasano, J. M.: Mediterranean intense desert dust outbreaks and their vertical structure based on remote sensing data, Atmos. Chem. Phys., 16, 8609–8642, https://doi.org/10.5194/acp-16-8609-2016, 2016.

Gkikas, A., Proestakis, E., Amiridis, V., Kazadzis, S., Di Tomaso, E., Tsekeri, A., Marinou, E., Hatzianastassiou, N., and Pérez García-Pando, C.: ModIs Dust AeroSol (MIDAS): a global fine-resolution dust optical depth data set, Atmos. Meas. Tech., 14, 309–334, https://doi.org/10.5194/amt-14-309-2021, 2021a.

Gkikas, A., Proestakis, E., Amiridis, V., Kazadzis, S., Di Tomaso, E., Marinou, E., Hatzianastassiou, N., Kok, J. F., and García-Pando, C. P.: Quantification of the dust optical depth across spatiotemporal scales with the MIDAS global dataset (2003–2017), Atmos. Chem. Phys. Discuss. [preprint], https://doi.org/10.5194/acp-2021-572, in review, 2021b.

Gläser, G., Wernli, H., Kerkweg, A., and Teubler, F.: The transatlantic dust transport from North Africa to the Americas-Its characteristics and source regions, J. Geophys. Res.-Atmos., 120, 11231–11252, https://doi.org/10.1002/2015JD023792, 2015.

Goudie, A.S. and Middelton, N.J.: Desert Dust in the Global System, Springer, 2006.

Griffin, D. W., Kellogg, C. A., Garrison, V. H., and Shinn, E. A.: The global transport of dust. An intercontinental river of dust, microorganisms and toxic chemicals flows through the Earth’s atmosphere, Am. Sci., 90, 228–235, 2002.

Guo, J., Xu, H., Liu, L., Chen, D., Peng, Y., Yim, S. H. L., Yang, Y., Li, J., Zhao, C., and Zhai, P.: The trend reversal of dust aerosol over East Asia and the North Pacific Ocean attributed to large-scale meteorology, deposition and soil moisture, J. Geophys. Res.-Atmos., 124, 10450–10466, https://doi.org/10.1029/2019JD030654, 2019

Guo, J. P., Zhang, X. Y., Wu, Y. R., Zhaxi, Y., Che, H. Z., La, B., Wang, W. and Li, X. W.: Spatio-temporal variation trends of satellite-based aerosol optical depth in China during 1980-2008, Atmos. Environ., 45(37), 6802–6811, https://doi.org/10.1016/j.atmosenv.2011.03.068, 2011.

Hamill, P., Giordano, M., Ward, C., Giles, D., and Holben, B.: An AERONET-based aerosol classification using the Mahalanobis distance, Atmos. Environ., 140, 213–233, https://doi.org/10.1016/j.atmosenv.2016.06.002, 2016.

Hammer, M. S., Martin, R. V., Li, C., Torres, O., Manning, M., and Boys, B. L.: Insight into global trends in aerosol composition from 2005 to 2015 inferred from the OMI Ultraviolet Aerosol Index, Atmos. Chem. Phys., 18, 8097–8112, https://doi.org/10.5194/acp-18-8097-2018, 2018.

Hersbach, H., Bell, B., Berrisford, P., Biavati, G., Horányi, A., Muñoz Sabater, J., Nicolas, J., Peubey, C., Radu, R., Rozum, I., Schepers, D., Simmons, A., Soci, C., Dee, D., and Thépaut, J.-N.: ERA5-Land hourly data from 1981 to present, Copernicus Climate Change Service (C3S) Climate Data Store (CDS) [data set], https://doi.org/10.24381/cds.adbb2d47, 2018.

Hersbach, H., Bell, B., Berrisford, P., Hirahara, S., Horányi, A., Muñoz-Sabater, J., Nicolas, J., Peubey, C., Radu, R., Schepers, D., Simmons, A., Soci, C., Abdalla, S., Abellan, X., Balsamo, G., Bechtold, P., Biavati, G., Bidlot, J., Bonavita, M., De Chiara, G., Dahlgren, P., Dee, D., Diamantakis, M., Dragani, R., Flemming, J., Forbes, R., Fuentes, M., Geer, A., Haimberger, L., Healy, S., Hogan, R. J., Hólm, E., Janisková, M., Keeley, S., Laloyaux, P., Lopez, P., Lupu, C., Radnoti, G., de Rosnay, P., Rozum, I., Vamborg, F., Villaume, S., and Thépaut, J.-N.: The ERA5 global reanalysis, Q. J. Roy. Meteor. Soc., 146, 1999–2049, https://doi.org/10.1002/qj.3803, 2020.

Holben, B. N., Eck, T. F., Slutsker, I., Tanre, D., Buis, J. P., Setzer, A., Vermote, E., Reagan, J. A., Kaufman, Y., Nakajima, T., Lavenue, F., Jankowiak, I., and Smirnov, A.: AERONET – A federated instrument network and data archive for aerosol characterization, Remote Sens. Environ., 66, 1–16, https://doi.org/10.1016/S0034-4257(98)00031-5, 1998.

Hsu, N. C., Gautam, R., Sayer, A. M., Bettenhausen, C., Li, C., Jeong, M. J., Tsay, S.-C., and Holben, B. N.: Global and regional trends of aerosol optical depth over land and ocean using SeaWiFS measurements from 1997 to 2010, Atmos. Chem. Phys., 12, 8037–8053, https://doi.org/10.5194/acp-12-8037-2012, 2012.

Hu, K., Kumar, K. R., Kang, N., Boiyo, R. and Wu, J.: Spatiotemporal characteristics of aerosols and their trends over mainland China with the recent Collection 6 MODIS and OMI satellite datasets, Environ. Sci. Pollut. Res., 25(7), 6909–6927, https://doi.org/10.1007/s11356-017-0715-6, 2018.

Huang, J., Zhang, C., and Prospero, J. M.: African dust outbreaks: a satellite perspective of temporal and spatial variability over the tropical Atlantic Ocean, J. Geophys. Res., 115, D05202, https://doi.org/10.1029/2009JD012516, 2010.

Jin, Q. and Wang, C.: The greening of Northwest Indian subcontinent and reduction of dust abundance resulting from Indian summer monsoon revival, Sci. Rep., 8(1), 1–9, https://doi.org/10.1038/s41598-018-23055-5, 2018.

Kalashnikova, O. V. and Kahn, R. A.: Mineral dust plume evolution over the Atlantic from MISR and MODIS aerosol retrievals, J. Geophys. Res., 113, D24204, https://doi.org/10.1029/2008JD010083, 2008.

Kaku, K. C., Reid, J. S., O'Neill, N. T., Quinn, P. K., Coffman, D. J., and Eck, T. F.: Verification and application of the extended spectral deconvolution algorithm (SDA+) methodology to estimate aerosol fine and coarse mode extinction coefficients in the marine boundary layer, Atmos. Meas. Tech., 7, 3399–3412, https://doi.org/10.5194/amt-7-3399-2014, 2014.

Klingmüller, K., Pozzer, A., Metzger, S., Stenchikov, G. L. and Lelieveld, J.: Aerosol optical depth trend over the Middle East, Atmos. Chem. Phys., 16(8), 5063–5073, https://doi.org/10.5194/acp-16-5063-2016, 2016.

Kok, J. F., Ridley, D. A., Zhou, Q., Miller, R. L., Zhao, C., Heald, C. L., Ward, D. S., Albani, S., and Haustein, K.: Smaller desert dust cooling effect estimated from analysis of dust size and abundance, Nat. Geosci., 10, 274–278, https://doi.org/10.1038/ngeo2912, 2017.

Kumar, K. R., Yin, Y., Sivakumar, V., Kang, N., Yu, X., Diao, Y., Adesina, A. J. and Reddy, R. R.: Aerosol climatology and discrimination of aerosol types retrieved from MODIS, MISR and OMI over Durban (29.88°S, 31.02°E), South Africa, Atmos. Environ., 117, 9–18, https://doi.org/10.1016/j.atmosenv.2015.06.058, 2015.

Kumar, K. R., Boiyo, R., Madina, A. and Kang, N.: A 13-year climatological study on the variations of aerosol and cloud properties over Kazakhstan from remotely sensed satellite observations, J. Atmos. Solar-Terrestrial Phys., 179, 55–68, https://doi.org/10.1016/j.jastp.2018.06.014, 2018.

Lakshmi, N. B., Babu, S. S. and Nair, V. S.: Recent Regime Shifts in Mineral Dust Trends over South Asia from Long-Term CALIPSO Observations, IEEE Trans. Geosci. Remote Sens., 57(7), 4485–4489, https://doi.org/10.1109/TGRS.2019.2891338, 2019.

Lee, J., Kim, J., Song, C. H., Chun, Y., Sohn, B. J., and Holben, B. N.: Characteristics of aerosol types from AERONET sunphotometer measurements, Atmos. Environ., 44, 3110–3117, 2010.

Levy, R. C., Leptoukh, G. G., Kahn, R., Zubko, V., Gopalan, A., and Remer, L. A.: A critical look at deriving monthly aerosol optical depth from satellite data, IEEE Transactions on Geoscience and Remote Sensing, 47, 2942–2956, https://doi.org/10.1109/TGRS.2009.2013842, 25, 2009.

Logothetis, S.-A., Salamalikis, V. and Kazantzidis, A.: Aerosol classification in Europe, Middle East, North Africa and Arabian Peninsula based on AERONET Version 3, Atmos. Res., 239, https://doi.org/10.1016/j.atmosres.2020.104893, 2020.

Logothetis, S.-A., Salamalikis, V. and Kazantzidis, A.: The impact of different aerosol properties and types on direct aerosol radiative forcing and efficiency using AERONET version 3, Atmos. Res., 250, https://doi.org/10.1016/j.atmosres.2020.105343, 2021.

Li, J., Carlson, B. E., Dubovik, O. and Lacis, A. A.: Recent trends in aerosol optical properties derived from AERONET measurements, Atmos. Chem. Phys., 14(22), 12271–12289, https://doi.org/10.5194/acp-14-12271-2014, 2014.

Mahowald, N., Albani, S., Kok, J. F., Engelstaeder, S., Scanza, R., Ward, D. S., and Flanner, M. G.: The size distribution of desert dust aerosols and its impact on the Earth system, Aeolian Res., 15, 53–71, https://doi.org/10.1016/j.aeolia.2013.09.002, 2014.

Mielonen, T., Arola, A., Komppula, M., Kukkonen, J., Koskinen, J., de Leeuw, G., and Lehtinen, K.: Comparison of CALIOP level 2 aerosol subtypes to aerosol types derived from AERONET inversion data, Geophys. Res. Lett., 36, L18804, https://doi.org/10.1029/2009gl039609, 2009.

Mona, L., Amodeo, A., Pandolfi, M., and Pappalardo, G.: Saharan dust intrusions in the Mediterranean area: Three years of Raman lidar measurements, J. Geophys. Res., 111, D16203, https://doi.org/10.1029/2005JD006569, 2006.

Mona, L., Liu, Z., Müller, D., Omar, A., Papayannis, A., Pappalardo, G., Sugimoto, N., and Vaughan, M.: Lidar Measurements for Desert Dust Characterization: An Overview, Adv. Meteorol., 2012, 356265, https://doi.org/10.1155/2012/356265, 2012.

Nabat, P., Somot, S., Mallet, M., Chiapello, I., Morcrette, J. J., Solmon, F., Szopa, S., Dulac, F., Collins, W., Ghan, S., Horowitz, L. W., Lamarque, J. F., Lee, Y. H., Naik, V., Nagashima, T., Shindell, D., and Skeie, R.: A 4-D climatology (1979–2009) of the monthly tropospheric aerosol optical depth distribution over the Mediterranean region from a comparative evaluation and blending of remote sensing and model products, Atmos. Meas. Tech., 6, 1287–1314, https://doi.org/10.5194/amt-6-1287-2013, 2013.

Ningombam, S. S., Larson, E. J. L., Dumka, U. C., Estellés, V., Campanelli, M. and Steve, C.: Long-term (1995–2018) aerosol optical depth derived using ground based AERONET and SKYNET measurements from aerosol aged-background sites, Atmos. Pollut. Res., 10(2), 608–620, https://doi.org/10.1016/j.apr.2018.10.008, 2019.

Notaro, M., Yu, Y., and Kalashnikova, O. V.: Regime shift in Arabian dust activity, triggered by persistent Fertile Crescent drought, J. Geophys. Res.-Atmos., 120, 10229–10249, https://doi.org/10.1002/2015JD023855, 2015.

O’Neill, N. T., Ignatov, A., Holben, B. N., and Eck, T. F.: The lognormal distribution as a reference for reporting aerosol optical depth statistics; Empirical tests using multi-year, multi-site AERONET Sunphotometer data, Geophys. Res. Lett., 27, 3333–3336, https://doi.org/10.1029/2000GL011581, 2000.

O'Neill, N. T., Dubovik, O., and Eck, T. F.: Modified Ångström coefficient for the characterization of sub-micrometer aerosols, Appl. Optics, 40, 2368–2375, https://doi.org/10.1364/AO.40.002368, 2001.

O'Neill, N. T., Eck, T. F., Smirnov, A., Holben, B. N., and Thulasiraman, S.: Spectral discrimination of coarse and fine mode optical depth, J. Geophys. Res., 108, 4559–4573, https://doi.org/10.1029/2002JD002975, 2003.

Papadimas, C. D., Hatzianastassiou, N., Mihalopoulos, N., Querol, X., and Vardavas, I.: Spatial and temporal variability in aerosol properties over the Mediterranean basin based on 6- year (2000–2006) MODIS data, J. Geophys. Res., 113, D11205, https://doi.org/10.1029/2007JD009189, 2008.

Papayannis, A., Amiridis, V., Mona, L., Tsaknakis, G., Balis, D., Bösenberg, J., Chaikovski, A., De Tomasi, F., Grigorov, I., Mattis,I., Mitev, V., Muller, D., Nickovic, S., Pérez, C., Pietruczuk, A., Pisani, G., Ravetta, F., Rizi, V., Sicard, M., Trickl, T., Wiegner, M., Gerding, M., Mamouri, R. E., D’Amico, G., and Pappalardo, G.: Systematic lidar observations of Saharan dust over Europe in the frame of EARLINET (2000–2002), J. Geophys. Res., 113, D10204, https://doi.org/10.1029/2007JD009028, 2008.

Pan, B., Wang, Y., Hu, J., Lin, Y., Hsieh, J.-S., Logan, T., Feng, X., Jiang, J. H., Yung, Y. L., and Zhang, R.: Impacts of Saharan Dust on Atlantic Regional Climate and Implications for Tropical Cyclones, Journal of Climate, 31, 7621-7644, 10.1175/jcli-d-16-0776.1, 2018.

Pandey, S. K., Vinoj, V., Landu, K. and Babu, S. S.: Declining pre-monsoon dust loading over South Asia: Signature of a changing regional climate, Sci. Rep., 7(1), 1–10, https://doi.org/10.1038/s41598-017-16338-w, 2017.

Pozzer, A., de Meij, A., Yoon, J., Tost, H., Georgoulias, A. K., and Astitha, M.: AOD trends during 2001–2010 from observations and model simulations, Atmos. Chem. Phys., 15, 5521–5535, https://doi.org/10.5194/acp-15-5521-2015, 2015.

Proestakis, E., Amiridis, V., Marinou, E., Georgoulias, A. K., Solomos, S., Kazadzis, S., Chimot, J., Che, H., Alexandri, G., Binietoglou, I., Daskalopoulou, V., Kourtidis, K. A., de Leeuw, G., and van der A, R. J.: Nine-year spatial and temporal evolution of desert dust aerosols over South and East Asia as revealed by CALIOP, Atmos. Chem. Phys., 18, 1337-1362, https://doi.org/10.5194/acp-18-1337-2018, 2018.

Prospero, J. M., Ginoux, P., Torres, O., Nicholson, S. E., and Gill, T. E.: Environmental characterization of global sources of atmospheric soil dust identified with the Nimbus 7 Total Ozone Mapping Spectrometer (TOMS) absorbing aerosol product, Rev. Geophys., 40, 2-1–2-31, https://doi.org/10.1029/2000RG000095, 2002.

Prospero, J. M. and Lamb, P. J.: African Droughts and Dust Transport to the Caribbean: Climate Change Implications, Science, 302, 1024–1027, https://doi.org/10.1126/science.1089915, 2003.

Prospero, J. M. and Mayol-Bracero, O. L.: Understanding the transport and impact of African dust on the Caribbean Basin, Bull. Am. Meteorol. Soc., 94(9), 1329–1337, https://doi.org/10.1175/BAMS-D-12-00142.1, 2013.

Prospero, J. M., Collard, F. X., Molinie, J., and Jeannot, A.: Characterizing the annual cycle of African dust transport to the Caribbean Basin and South America and its impact on the environment and air quality, Global Biogeochem. Cy., 28, 757–773, https://doi.org/10.1002/2013gb004802, 2014.

Rajot, J. L., Formenti, P., Alfaro, S., Desboeufs, K., Chevaillier, S., Chatenet, B., Gaudichet, A., Journet, E., Marticorena, B., Triquet, S., Maman, A., Mouget, N., and Zakou, A.: AMMA dust experiment: An overview of measurements performed during the dry season special observation period (SOP0) at the Banizoumbou (Niger) supersite, J Geophys Res-Atmos, 113, https://doi.org/10.1029/2008JD009906, 2008.

Rashki, A., Kaskaoutis, D. G., Francois, P., Kosmopoulos, P. G. and Legrand, M.: Dust-storm dynamics over Sistan region, Iran: Seasonality, transport characteristics and affected areas, AEOLIAN Res., 16, 35–48, https://doi.org/10.1016/j.aeolia.2014.10.003, 2015.

Remer, L. A., Kleidman, R. G., Levy, R. C., Kaufman, Y. J., Tanré, D., Mattoo, S., Martins, J. V., Ichoku, C., Koren, I., Yu, H., and Holben, B. N.: Global aerosol climatology from the MODIS satellite sensors, J. Geophys. Res.-Atmos., 113, d14S07, https://doi.org/10.1029/2007JD009661, 2008.

Sayer, A. M. and Knobelspiesse, K. D.: How should we aggregate data? Methods accounting for the numerical distributions, with an assessment of aerosol optical depth, Atmos. Chem. Phys., 19, 15023–15048, https://doi.org/10.5194/acp-19-15023-2019, 2019.

Schepanski, K.: Transport of mineral dust and its impact on climate, Geosciences, 8, 151, https://doi.org/10.3390/geosciences8050151, 2018.

Shikwambana, L. and Sivakumar, V.: Global distribution of aerosol optical depth in 2015 using CALIPSO level 3 data, J. Atmos. Solar-Terrestrial Phys., 173, 150–159, https://doi.org/10.1016/j.jastp.2018.04.003, 2018.

Shi, L., Zhang, J., Yao, F., Zhang, D. and Guo, H.: Drivers to dust emissions over dust belt from 1980 to 2018 and their variation in two global warming phases. Sci. Total Environ., 767, 144860, https://doi.org/10.1016/j.scitotenv.2020.144860, 2021.

Song, Q., Zhang, Z., Yu, H., Ginoux, P., and Shen, J.: Global dust optical depth climatology derived from CALIOP and MODIS aerosol retrievals on decadal timescales: regional and interannual variability, Atmos. Chem. Phys., 21, 13369–13395, https://doi.org/10.5194/acp-21-13369-2021, 2021.

Textor, C., Schulz, M., Guibert, S., Kinne, S., Balkanski, Y., Bauer, S., Berntsen, T., Berglen, T., Boucher, O., Chin, M., Dentener, F., Diehl, T., Easter, R., Feichter, H., Fillmore, D., Ghan, S., Ginoux, P., Gong, S., Grini, A., Hendricks, J., Horowitz, L., Huang, P., Isaksen, I., Iversen, I., Kloster, S., Koch, D., Kirkevåg, A., Kristjansson, J. E., Krol, M., Lauer, A., Lamarque, J. F., Liu, X., Montanaro, V., Myhre, G., Penner, J., Pitari, G., Reddy, S., Seland, Ø., Stier, P., Takemura, T., and Tie, X.: Analysis and quantification of the diversities of aerosol life cycles within AeroCom, Atmos. Chem. Phys., 6, 1777–1813, https://doi.org/10.5194/acp-6-1777-2006, 2006.

Todd, M.C., Washington, R., Martins, J.V., Dubovik, O., Lizcano, G., M’Bainayel, S., Engelstaedter, S.: Mineral dust emission from the Bodélé Depression nothern Chad, during BoDEx 2005, J. Geophys. Res. Atmos., 112, 1–12, https://doi.org/10.1029/2006JD007170, 2007.

Torres, O., Bhartia, P. K., Herman, J. R., Sinyuk, A., Ginoux, P., and Holben, B.: A long-term record of aerosol optical depth from TOMS observations and comparison to AERONET measurements, J. Atmos. Sci., 59, 398–413, https://doi.org/10.1175/1520- 0469(2002)0592.0.CO;2, 2002.

Tsamalis, C., Chédin, A., Pelon, J., and Capelle, V.: The seasonal vertical distribution of the Saharan Air Layer and its modulation by the wind, Atmos. Chem. Phys., 13, 11235–11257, https://doi.org/10.5194/acp-13-11235-2013, 2013.

Voss, K. K., and Evan, A. T.: A new satellite-based global climatology of dust aerosol optical depth, Journal of Applied Meteorology and Climatology, https://doi.org/10.1175/JAMC-D-19-0194.1, 2020.

Washington, R., Todd, M.C., Engelstaedter, S., Mbainayel, S., Mitchell, F.: Dust and the low-level circulation over the Bodélé Depression, Chad: Observations from BoDEx 2005, J. Geophys. Res. Atmos., 111, 1–15, https://doi.org/10.1029/2005JD006502, 2006.

Weatherhead, E. C., Reinsel, G. C., Tiao, G. C., Meng, X.-L., Choi, D., Cheang, W.-K., Keller, T., DeLuisi, J., Wuebbles, D. J., Kerr, J. B., Miller, A. J., Oltmans, S. J., and Frederick, J. E.: Factors affecting the detection of trends: Statistical considerations and applications to environmental data, J. Geophys. Res., 103(D14), 17149–17161, https://doi.org/10.1029/98JD00995,1998.

van der Does, M., Knippertz, P., Zschenderlein, P., Harrison, R. G., and Stuut, J. B. W.: The mysterious long-range transport of giant mineral dust particles, Sci. Adv., 4, eaau2768, https://doi.org/10.1126/sciadv.aau2768, 2018.

Wei, J., Peng, Y., Mahmood, R., Sun, L., and Guo, J.: Intercomparison in spatial distributions and temporal trends derived from multi-source satellite aerosol products, Atmos. Chem. Phys., 19, 7183–7207, https://doi.org/10.5194/acp-19-7183-2019, 2019a.

Wei, J., Li, Z., Peng, Y., and Sun, L.: MODIS Collection 6.1 aerosol optical depth products over land and ocean: validation and comparison, Atmos. Environ., 201, 428–440, 2019b.

Xi, X. and Sokolik, I. N.: Dust interannual variability and trend in Central Asia from 2000 to 2014 and their climatic linkages, J. Geophys. Res., 120, 12175–12197, https://doi.org/10.1002/2015JD024092, 2015.

Xian, P., Klotzbach, P. J., Dunion, J. P., Janiga, M. A., Reid, J. S., Colarco, P. R., and Kipling, Z.: Revisiting the relationship between Atlantic dust and tropical cyclone activity using aerosol optical depth reanalyses: 2003–2018, Atmos. Chem. Phys., 20, 15357–15378, https://doi.org/10.5194/acp-20-15357-2020, 2020.

Yoon, J., Burrows, J. P., Vountas, M., von Hoyningen-Huene, W., Chang, D. Y., Richter, A., and Hilboll, A.: Changes in atmospheric aerosol loading retrieved from space-based measurements during the past decade, Atmos. Chem. Phys., 14, 6881–6902, https://doi.org/10.5194/acp-14-6881-2014, 2014.

Yu, Y., Notaro, M., Liu, Z., Wang, F., Alkolibi, F., Fadda, E., and Bakhrjy, F.: Climatic controls on the interannual to decadal variability in Saudi Arabian dust activity: Toward the development of a seasonal dust prediction model, J. Geophys. Res.-Atmos., 120, 1739–1758, https://doi.org/10.1002/2014JD022611, 2015.

Yu, H., Tan, Q., Chin, M., Remer, L. A., Kahn, R. A., Bian, H., Kim, D., Zhang, Z., Yuan, T., Omar, A. H., Winker, D. M., Levy, R. C., Kalashnikova, O., Crepeau, L., Capelle, V., and Chedin, A.: Estimates of African dust deposition along the trans-Atlantic transit using the decade-long record of aerosol measurements from CALIOP, MODIS, MISR, and IASI, J. Geophys. Res.-Atmos., 124, 7975–7996, https://doi.org/10.1029/2019JD030574, 2019.

Zender, C. S., Miller, R., and Tegen, I.: Quantifying mineral dust mass budgets: Terminology, constraints, and current estimates, Eos, Transactions American Geophysical Union, 85, 509–512, https://doi.org/10.1029/2004EO480002, 2004.

Zhang, J. and Reid, J. S.: A decadal regional and global trend analysis of the aerosol optical depth using a data-assimilation grade over-water MODIS and Level 2 MISR aerosol products, Atmos. Chem. Phys., 10, 10949–10963, https://doi.org/10.5194/acp-10-10949-2010, 2010.

Zhang, M., Wang, Y., Ma, Y., Wang, L., Gong, W. and Liu, B.: Spatial distribution and temporal variation of aerosol optical depth and radiative effect in South China and its adjacent area, Atmos. Environ., 188, 120–128, https://doi.org/10.1016/j.atmosenv.2018.06.028, 2018.

Zhao, B., Jiang, J. H., Gu, Y., Diner, D., Worden, J., Liou, K. N., Su, H., Xing, J., Garay, M., and Huang, L.: Decadal-scale trends in regional aerosol particle properties and their linkage to emission changes, Environ. Res. Lett, 12, 054021, https://doi.org/10.1088/1748-9326/aa6cb2, 2017.